

Supplementary information

**Images of embedded Jovian planet
formation at a wide separation around AB
Aurigae**

In the format provided by the
authors and unedited

Supplementary Information for

Images of Embedded Jovian Planet Formation At Wide Separations Around AB Aurigae

Thayne Currie^{1,2,3}, Kellen Lawson⁴, Glenn Schneider⁵, Wladimir Lyra⁶, John Wisniewski⁴, Carol Grady³, Olivier Guyon^{1,5,7}, Motohide Tamura^{7,8,9}, Takayuki Kotani^{7,8}, Hajime Kawahara¹⁰, Timothy Brandt¹¹, Taichi Uyama¹², Takayuki Muto¹³, Ruobing Dong¹⁴, Tomoyuki Kudo¹, Jun Hashimoto⁸, Misato Fukagawa⁸, Kevin Wagner^{5,15}, Julien Lozi¹, Jeffrey Chilcote¹⁶, Taylor Tobin¹⁶, Tyler Groff¹⁷, Kimberly Ward-Duong¹⁸, William Januszewski¹⁸, Barnaby Norris¹⁹, Peter Tuthill¹⁹, Nienke van der Marel²⁰, Michael Sitko²¹, Vincent Deo¹, Sebastien Vievard^{1,7}, Nemanja Jovanovic²², Frantz Martinache²³, Nour Skaf¹

¹ Subaru Telescope, National Astronomical Observatory of Japan, Hilo, HI, USA.

²NASA-Ames Research Center, Moffett Field, CA, USA. ³Eureka Scientific, Oakland, CA, USA. ⁴Homer L. Dodge Department of Physics and Astronomy, University of Oklahoma, OK, USA. ⁵Steward Observatory, The University of Arizona, Tucson, AZ.

⁶Department of Physics and Astronomy, New Mexico State University, NM, USA.

⁷Astrobiology Center, Tokyo, Japan. ⁸National Astronomical Observatory of Japan, Tokyo, Japan. ⁹Department of Astronomy, Graduate School of Science, The University of Tokyo, Tokyo, Japan. ¹⁰Department of Earth and Planetary Sciences, University of Tokyo, Tokyo, Japan. ¹¹Department of Physics and Astronomy, University of California-Santa Barbara, CA, USA. ¹²Infrared Processing and Analysis Center,

California Institute of Technology, Pasadena, CA, USA. ¹³Division of Liberal Arts, Kogakuin University, Tokyo, Japan. ¹⁴Department of Astronomy, University of Victoria, Victoria, BC, Canada. ¹⁵NASA Hubble Fellowship Program – Sagan Fellow.

¹⁶Department of Physics, University of Notre Dame, Notre Dame, IN, USA. ¹⁷NASA-Goddard Spaceflight Center, Greenbelt, MD, USA. ¹⁸Space Telescope Science Institute, Baltimore, MD, USA. ¹⁹Sydney Institute for Astronomy, School of Physics, University of Sydney, Australia. ²⁰Leiden Observatory, Leiden, Netherlands. ²¹Space Science Institute, Boulder, CO, USA. ²²Department of Astronomy, California Institute of Technology, Pasadena, CA, USA. ²³Université Côte d'Azur, Observatoire de la Côte d'Azur, CNRS, Laboratoire Lagrange, Nice, France. e-mail: currie@naoj.org

S1. Robust Detection of AB Aur b

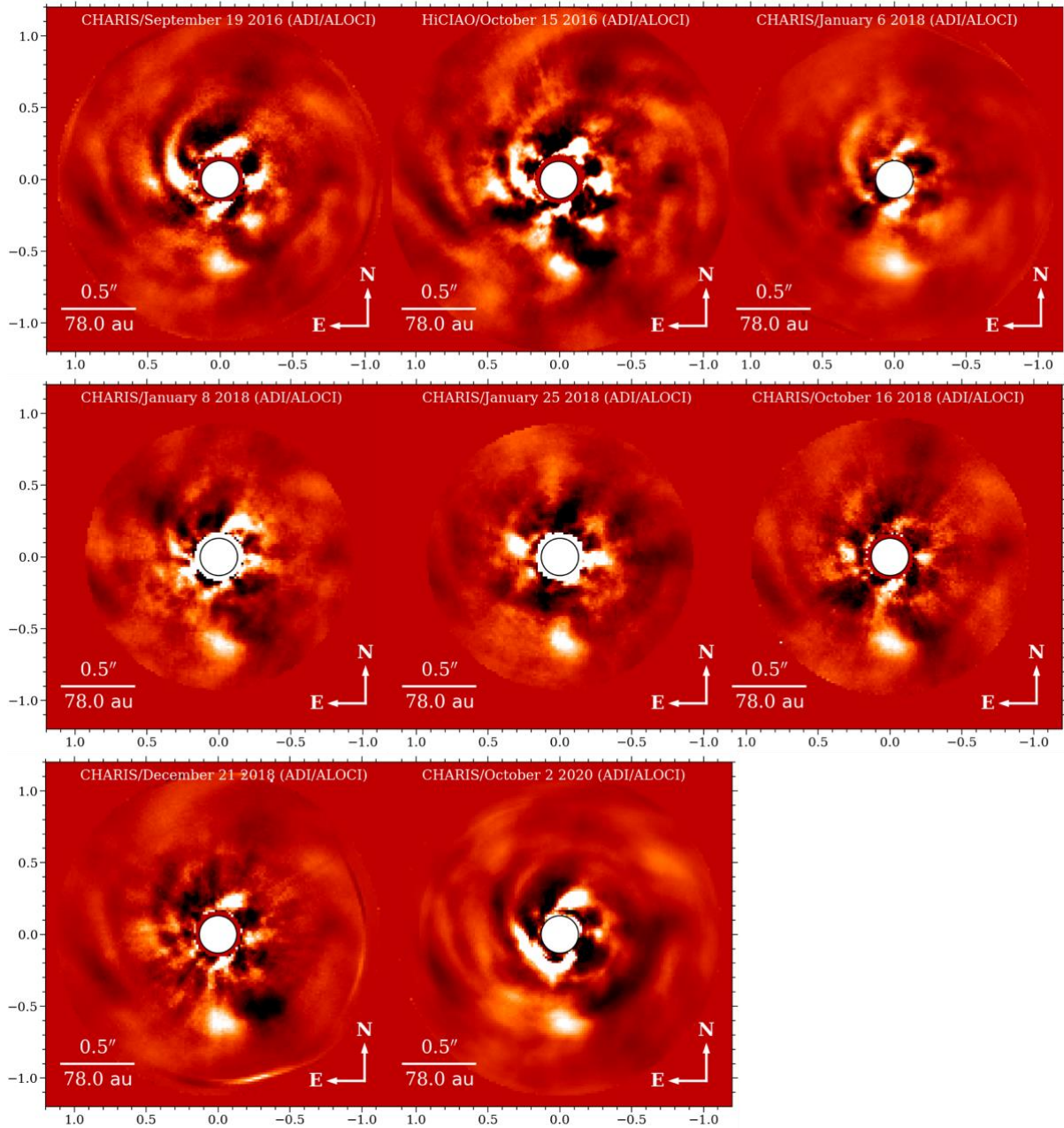
Supplementary Table 1 displays our full observing log. Below we add further details describing the detection of AB Aur b from ground based data and HST data.

Supplementary Table 1 | Observing Log

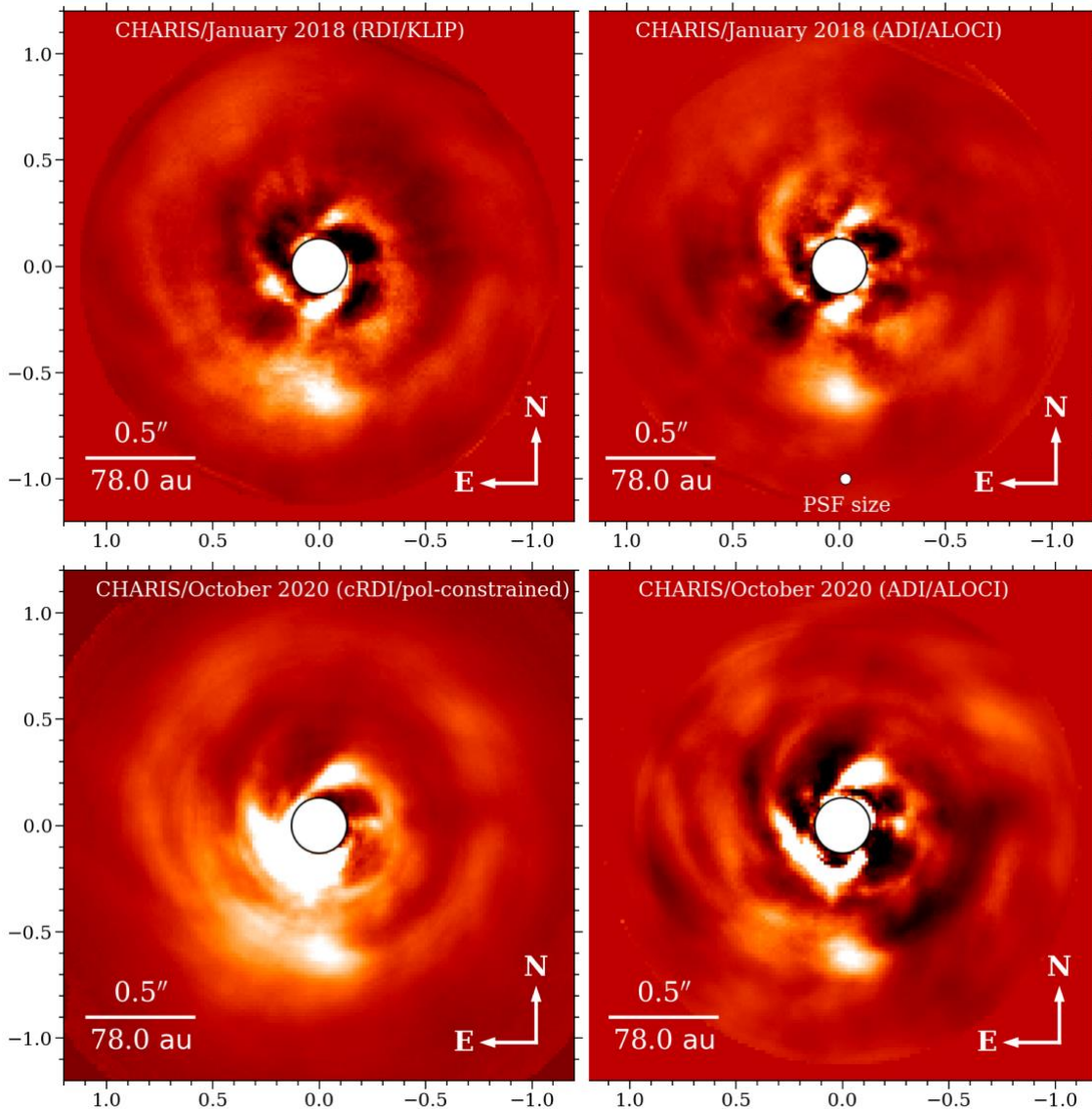
UT Date	Instrument	Natural Seeing (")	Passband	λ (μm)	t_{exp} (s)	N_{exp}	ΔPA ($^{\circ}$)	Observing/Reduction Strategy
New Data								
20160918	SCEXAO/CHARIS	0.3	JHK	1.16-2.39	45	60	60	ADI
20161015	SCEXAO/HiCIAO	0.6	JHK	1.65	30	41	45	ADI,RDI
20180106	SCEXAO/CHARIS	0.5	JHK	1.16-2.39	45	60	110	ADI,RDI
20180108	SCEXAO/CHARIS	1.2	JHK	1.16-2.39	45	60	110	ADI
20180125	SCEXAO/CHARIS	1.5	JHK	1.16-2.39	31	199	143	ADI
20181016	SCEXAO/CHARIS	0.6	JHK	1.16-2.39	60.5	46	63	ADI
20181101	Keck/NIRC2	0.7	Lp	3.78	50	120	132	ADI
20181221	SCEXAO/CHARIS	0.9	JHK	1.16-2.39	20.6	162	53	ADI
20201002	SCEXAO/CHARIS	0.4-0.7	JHK	1.16-2.39	31	130	127	ADI,RDI
20201002	SCEXAO/VAMPIRES	-	H α /Cont	0.64-0.66	72.1	51	136	ADI,RDI
20201003	SCEXAO/CHARIS	0.6-0.8	JHK-pol	1.16-2.39	60.5	73	80	PDI
20210104	HST/STIS	-	50CCD	0.2--1	56	27	6	RDI
20210207	HST/STIS	-	50CCD	0.2--1	56	18	4	RDI
Archival Data								
19990123	HST/STIS	-	50CCD	0.2--1	576	6	22.2	RDI
20071221-20070914	HST/NICMOS	-	F110W	1.10	511.6	2	137	RDI
20071221-20070914	HST/NICMOS	-	POL0	2.05	192.0	18	137	PDI,RDI
20070914	-	-	120/240	-	-	-	-	-

Ground-Based Near-IR Total Intensity Data

Supplementary Figure 1 shows a gallery of ground-based images obtained with SCEXAO/CHARIS and SCEXAO/HiCIAO, reduced with ADI/ALOCI. For each image, the intensity scaling is normalized to the peak emission of AB Aur b. The detection of spiral features at small angular separations ($\sim 0.2''$) depends on the quality of a given data set. However, we clearly detect AB Aur b at $\rho \sim 0.6''$ in each case.

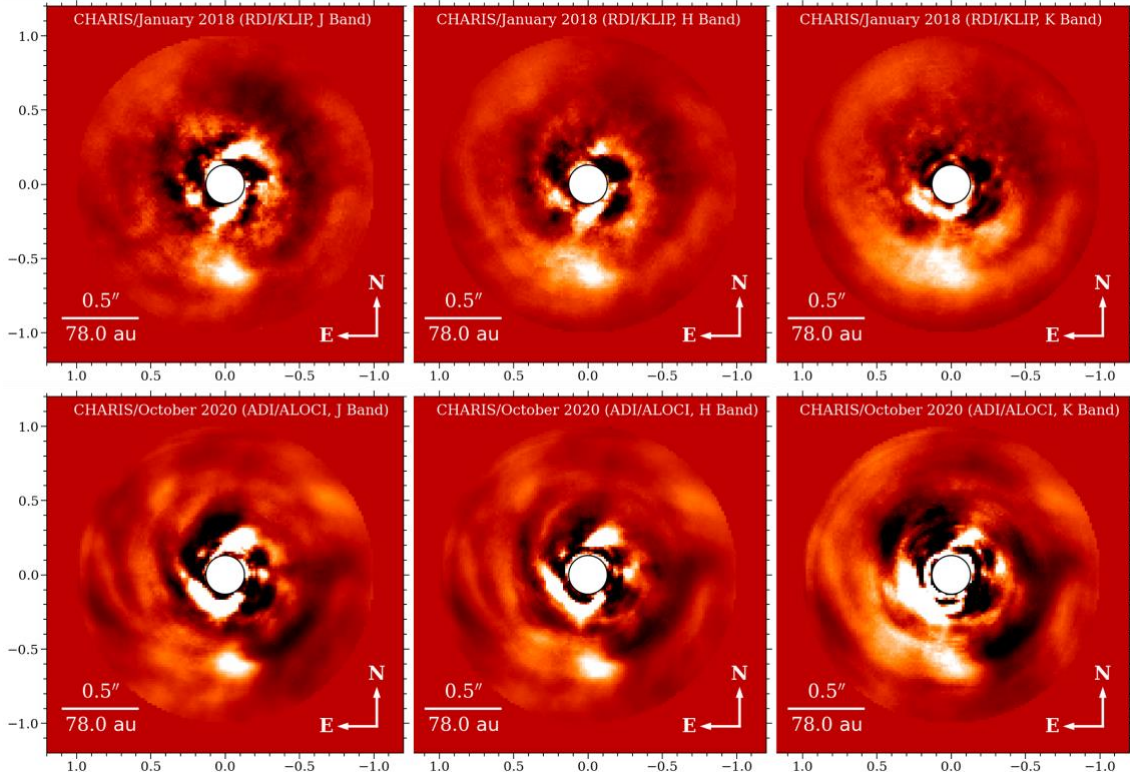


Supplementary Figure 1 – Gallery of CHARIS and HiCIAO images of AB Aur (ADI/ALOCI reductions). The data quality varies substantially from “excellent” (January 6, 2018; October 2, 2020) to “poor” (January 8 and 25, 2018), impeding our ability to consistently detect the inner spirals. However, AB Aur b is detected in all data sets. The panel intensity scales in units of mJy. Quantitatively, these values are (left to right, top to bottom) [-0.0375, 0.0375], [-0.004, 0.004], [-0.065, 0.065], [-0.16, 0.16], [-0.18, 0.18], [-0.045, 0.045], [-0.0375, 0.0375], and [-0.0375, 0.0375]. The scaling for the two poorer-quality data sets is numerically larger because the flux calibration was done in a FWHM-sized aperture, not with a constant size.



Supplementary Figure 2 – CHARIS AB Aur data from January 2018 (top) and October 2020 (bottom) reduced using algorithms in combination with RDI (left panels) and ADI (right panels). RDI reductions better preserve low surface brightness disk features, while ADI/ALOCI reductions better reveal spiral structure at the cost of self-subtraction at the smallest angular separations. The January 2018 ADI/ALOCI reduction is the same one shown in Figure 1 (left panel); the October 2020 cRDI/pol-constrained reduction is the same one shown in Figure 1 (right panel). All reductions clearly show AB Aur b. The filled white circle in the top-right panel shows the approximate PSF core size: AB Aur b is spatially resolved.

AB Aur b is visible and morphologically consistent in each SCEXAO image regardless of whether we use ADI or RDI, ALOCI or KLIP (Figures S2 and S3). Generally speaking, ADI-ALOCI and ADI-KLIP yield higher SNR detections but act as better high-pass filters, significantly attenuating relatively flat emission from the disk, and sharpening their morphologies. PSF subtraction used in combination with RDI better preserve emission from the disk and in general yields a higher fidelity image of the astrophysical scene at the cost of more poorly suppressing speckle noise, especially at angular separations interior to AB Aur b.



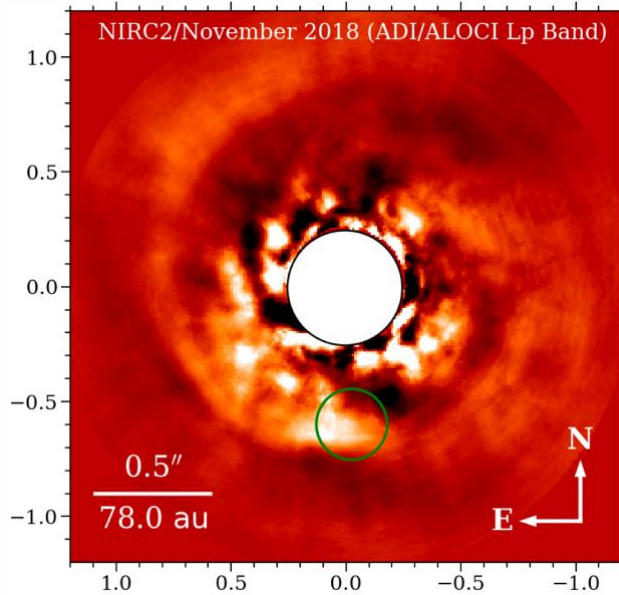
Supplementary Figure 3 – The final J, H, and K images from CHARIS AB Aur data from January 2018 reduced with RDI/KLIP (top) and October 2020 reduced with ADI/ALOCI (bottom). AB Aur b is plainly visible in J and H bands. At Ks band, its signal starts to become contaminated by the the disk.

Supplementary Figure 3 shows how the detectability of AB Aur b varies across J, H, and Ks passbands in the January 2018 RDI/KLIP and October 2020 ADI/ALOCI reduced data. At J band, AB Aur b’s signal stands out clearly, its peak signal is roughly 4--5 brighter than the per-pixel average signal flanking disk regions in the RDI-reduced data. It is still clearly visible in H at ~ 2.5 times the disk brightness, although the disk background signal is larger in relative brightness. At Ks band, AB Aur b becomes contaminated by and is more difficult to distinguish from the disk. Only ADI reductions yield a clear signal in the longest wavelength channels in both data sets. These results are consistent with AB Aur b being an object with bluer near-IR colors than those expected from scattered starlight, whose SED resembles that of a ~ 1400 K blackbody¹.

We fail to decisively detect AB Aur b in the thermal IR (L_p) with Keck/NIRC2 (Supplementary Figure 4). These data were taken with a poorer AO correction than that from most SCEXAO data sets, although we do convincingly detect the ring of emission seen in submm data as well as the inner spirals; high humidity (near $\sim 80\%$) also reduced thermal IR sensitivity at wide separations. A small subset of alternate, aggressive ADI reductions (not shown) do show a concentrated emission clump similar in spatial extent and location to b albeit at marginal significance ($\sim 2\sigma$). Using more conservative reductions (shown) that better preserve disk features seen with other instruments leaves a non-detection (dashed circle). Likewise, it is not recovered in an RDI reduction. We

also reduced other AB Aur Lp data sets from the Keck Observatory Archive, also failing to yield a detection.

Thus, we consider only $5\text{-}\sigma$ upper limits for the detection of AB Aur b at Lp. Future thermal IR observations with the recently-upgraded Keck II AO system or with the James Webb Space Telescope are needed to detect or place better limits on AB Aur b in the thermal IR.



Supplementary Figure 4 – Keck/NIRC2 Lp image of AB Aur. A poorer AO correction (more variable, not diffraction limited), higher thermal background, and brighter disk explain to our failure to recover AB Aur b in these data (position circled).

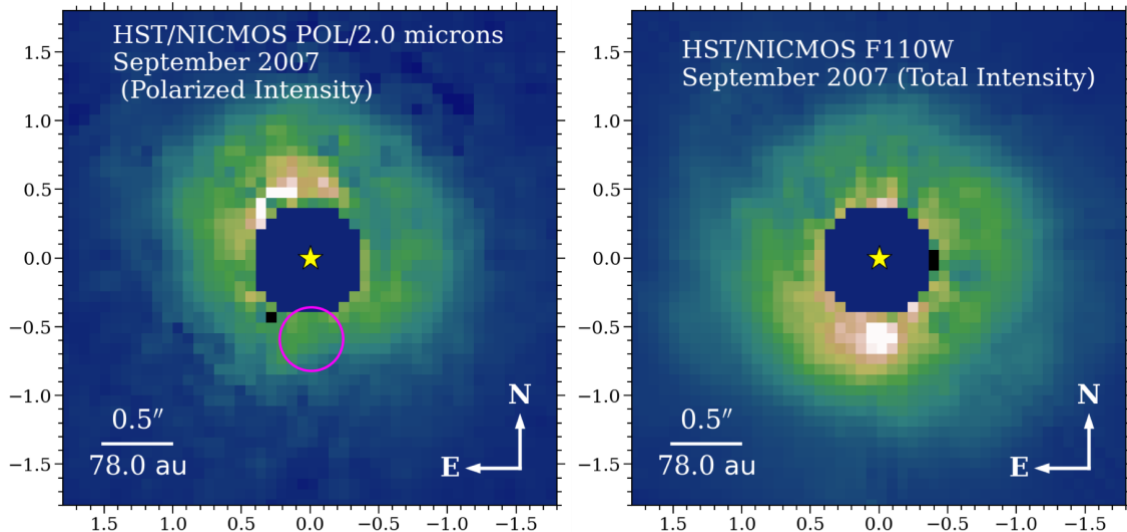
Ground-Based Optical Data

The VAMPIRES data were obtained in two cameras and split the continuum bandpass ($0.64\ \mu\text{m}$; 2nm wide) and the narrow $\text{H}\alpha$ filter ($0.653\ \mu\text{m}$; 1nm wide). We found that camera 1 yielded far more sensitive data, and thus we focus on these data. To precisely flux-calibrate these data, we used the empirical AB Aur spectrum² and computed the average flux density for wavelengths covering the continuum and narrow band filters. We estimate a flux density of $\sim 5.2\ \text{Jy}$ in the continuum and $\sim 12.56\ \text{Jy}$ at $\text{H}\alpha$ for the star.

As VAMPIRES' astrometric solution had not previously been calibrated, we constructed an approximate astrometric solution based off of recent observations of systems observed simultaneously with CHARIS: primarily based on binary companions at $\sim 0.3''$ separations and the HD 1160 B brown dwarf. Based on these comparisons, we estimate a VAMPIRES pixel scale of $6.24 \pm 0.01\ \text{mas/pixel}$, yielding a field-of-view of $\sim 0.8''$ in radius. We computed a north position angle offset from the detector y position of $78.6 \pm 1.2\ \text{degrees}$. The VAMPIRES detector likely has distortion on the order of \sim a few pixels at the separation of AB Aur b, which we do not correct for: we

have found no evidence so far that CHARIS suffers from astrometric distortion at a level that could impact our results.

We explored multiple approaches to reduce VAMPIRES data. Prior H α detections of protoplanet candidates either differenced ADI-reduced H α and continuum images or exploited high-resolution spectroscopy to detect the lines from SDI alone³⁻⁴. The VAMPIRES PSF was sufficiently stable to use HD 31233 as a PSF reference star and perform PSF subtraction using RDI with the KLIP algorithm. We also explored reducing VAMPIRES data with ADI in combination with the KLIP or ALOCI algorithms. Both RDI and ADI approaches yielded clear detections of AB Aur b (SNR ~ 5 – 5.8). Considering both intrinsic astrometric calibration uncertainties and uncertainties due to centroiding and the intrinsic source SNR, we derive a position of $\rho = 0.598'' \pm 0.014''$, PA = $180.5^\circ \pm 2.2^\circ$. While not nearly as precise as other measurements, this position is consistent with contemporaneous CHARIS astrometry at the 1.4-sigma level. The RDI reduction results in $\sim 100\%$ throughput and no self-subtraction. Thus, we base our VAMPIRES photometry on these data.



Supplementary Figure 5 – HST/NICMOS 2.05 micron polarized intensity image for AB Aur. (left) compared to the F110W total intensity image (right). We detect no polarized signal at the position of AB Aur b (circled).

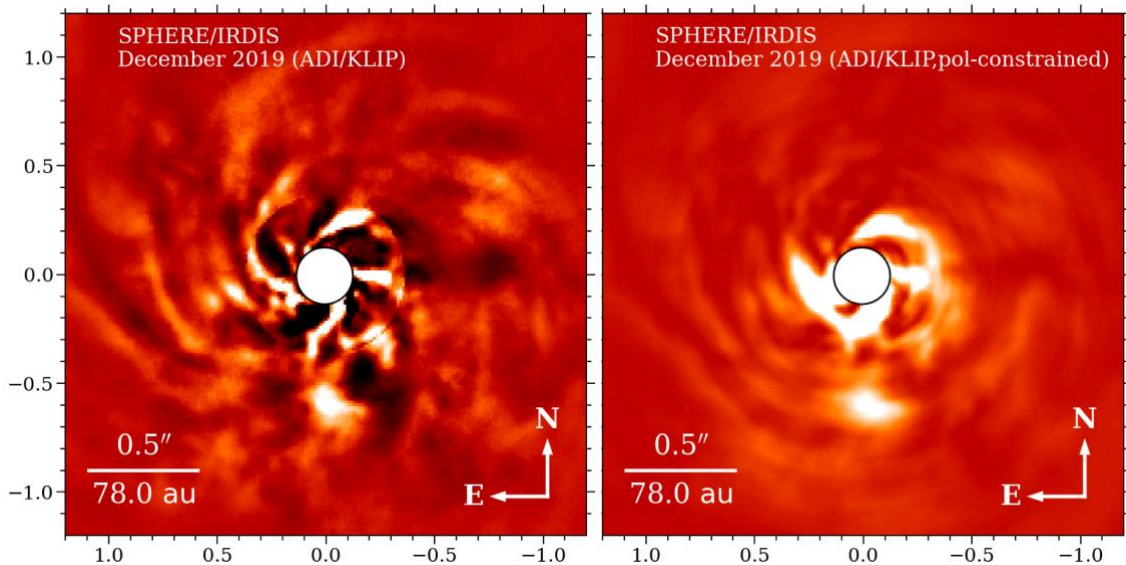
HST Total Intensity Data

AB Aur b is easily visible in the roll-combined F110W NICMOS data and is also separately detectable in the two individual rolls. The September 2007 NICMOS POL total intensity data (2.05 microns) also reveal what is potentially a detection of AB Aur b in the first roll position, albeit with substantial PSF subtraction residuals. However, the second, poorer quality roll position does not clearly reveal concentrated emission at this location. The roll-combined data therefore yields an ambiguous interpretation. Because the F110W NICMOS data yield an unambiguous detection, we focus on those data for photometry and astrometry.

Likewise, AB Aur b is easily visible in the roll-combined STIS images in both the January and February 2021 data sets, as well as individual PSF subtracted exposures. Comparing these data reveals some slight differences in the intensity distribution of the disk, suggesting possible variability. However, the signal of AB Aur b remains constant to within 10%. AB Aur b’s position lies underneath the coronagraph wedge in the 1999 reprocessed archival STIS data.

Additional Polarized Intensity Data

As shown in Figure 4 of the main paper, AB Aur b is a non-detection in CHARIS polarized intensity imaging. Inspection of the total and polarized intensity images shows that the raw count values of pixels in total intensity have a definable peak at AB Aur b’s position but are flat in polarized intensity. Supplementary Figure 5 likewise shows a non-detection of AB Aur b in HST/NICMOS polarimetry. Unpublished HiCIAO polarimetry of AB Aur likewise shows a detection of the disk but not AB Aur b.



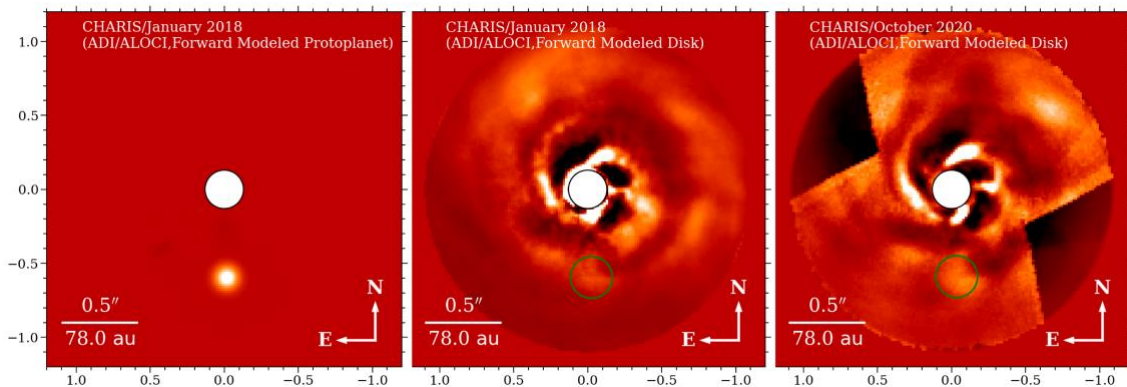
Supplementary Figure 6 – Reprocessed SPHERE/IRDIS H band image of AB Aur from December 2019. The data are reduced with ADI/KLIP (left) and “polarimetry-constrained” ADI/KLIP (right). AB Aur b is visible in both reductions.

Other Data Not Analyzed in this Work

In addition to the data presented in this paper, we searched for additional AB Aur data from the ground and space that could affect our conclusions. Archival data from Subaru/CIAO from 2004 are of poorer quality compared to both SCExAO and Keck/NIRC2 data. We do detect a concentrated signal at roughly $[E,N] = 0.05'', -0.60''$, which would be consistent with AB Aur b in the CIAO data reduced with classical PSF subtraction, although the signal is close to the mask edge/saturated portion of the image. Thus, we do not yet consider this to be a decisive detection. Archival NIRC2 Lp data from 2015 and obtained with the vortex coronagraph do not appear to improve upon our 2018 NIRC2 limits.

As a final check on our results, we downloaded and reprocessed recently published SPHERE/IRDIS total intensity and polarized intensity data for AB Aur from December 2019. While the AO performance for these data is close in quality to our best SCExAO data sets, these data were obtained without a PSF reference star and with poor field rotation making them more ill-suited for unambiguous detections and characterizations of AB Aur b. We processed these data with the IRDAP pipeline⁵. To PSF subtract the total intensity data, we used two approaches: ADI/KLIP and polarimetry-constrained PSF subtraction method with KLIP.

As shown in Supplementary Figure 6, these data support conclusions based on SCExAO data. AB Aur b is clearly detected in SPHERE total intensity data. We do not detect AB Aur b in polarized intensity. The position of AB Aur b is intermediate between values determined from the October 2018 and October 2020 data. Results from these data are discussed further in S8.



Supplementary Figure 7 – Forward-modeling of our AB Aur images. (left) Forward-model of a protoplanet through the January 2018 data: processing removes 10% of the light or less from this source. (middle) Forward-model of the Subaru/HiCIAO polarized intensity detection of the AB Aur disk through our CHARIS data; (right) forward-model of the SCExAO/CHARIS integral field polarimetry detection of the AB Aur disk through the CHARIS October 2020 data. The location of AB Aur b has a flat residual disk signal in both cases. Forward-modeling of the disk shows that our processing is not creating a point-like signal misidentified as a protoplanet. Note that the signals at the 10 o'clock and 4 o'clock positions from the AB Aur b positions are flat/constant, not concentrated. They are also at separations and position angles completely inconsistent with AB Aur b.

S2. Forward-Modeling and Spectral Modeling: AB Aur b is not a processing artefact

To assess and correct for flux attenuation of AB Aur b in CHARIS data due to processing, we first performed forward-modeling with ADI-ALOCI and RDI-KLIP following previous demonstrated approaches with SCExAO data⁶. Supplementary Figure 7 (left) shows the forward-modeled PSF. The post-forward modelling signal from AB Aur b matches the input PSF, suggesting only minor reduction of its signal, consistent with the high throughputs (90-99%) listed in Methods. Similarly, we found negligible astrometric biasing due to processing in these data sets.

To assess how the source throughput depends on the assumed source morphology and intensity distribution, we performed forward-modeling on an unresolved point source, an 8-pixel wide (or 16 pixel-wide for HiCIAO) constant intensity source ($\theta \sim 0.13''$), and other intensity distributions. In all cases, signal loss at AB Aur b's location is negligible, less than 10%. Significant spectrophotometric and astrometric biasing only occurs for more aggressive reductions: e.g. PSF subtraction performed in small annular wedges instead of over the entire field at once or smaller rotation gaps.

Advanced PSF subtraction methods have the potential to break up continuous disk features to make them appear like planets⁷. To test this possibility with our SCEXAO/CHARIS data, we adopted the polarimetry data as a disk model and then used forward-modeling techniques to simulate the appearance of these data (containing the polarized light detection of the disk) in the total intensity data. As shown in Supplementary Figure 7 (middle, right), AB Aur b cannot be a processing artefact: the forward-modeled disk image lacks a detectable concentrated signal at the companion's location. As a second test, we forward-modeled both the CHARIS and unpublished HiCIAO H band polarimetry data from 2016 through our January 2018 CHARIS data. These analysis yields identical results: the forward-modeled disk image shows no peaked signal at the position of AB Aur b.

Optimized PCRDI - Finally, we employ polarimetry-constrained classical reference star differential imaging (PCRDI) on the October 2020 data as an additional test. PCRDI is summarized in Methods. We give more detail below.

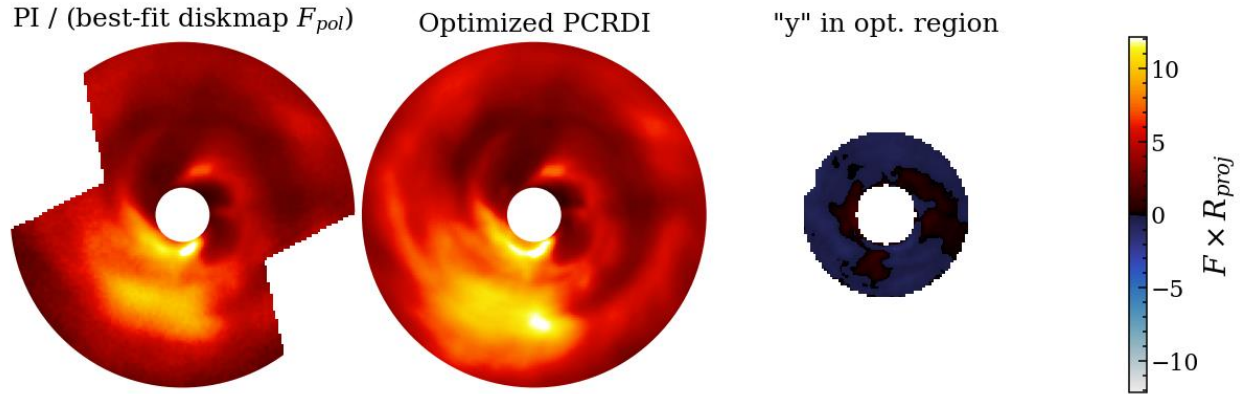
Let I_{est} be the total intensity estimate determined from PI and a particular set of diskmap parameters describing a smooth scattering surface ($h(r) = a+br^c$) with a particular peak fractional polarization (s), viewed at a particular orientation (incl, PA). Let $T_{D,\text{est}}$ be the sequence of I_{est} rotated to the parallactic angles to match the target sequence, T , such that $T - T_{D,\text{est}}$ is our estimate of the target sequence containing only starlight.

Let $M(T, R)$ be the PSF model for T based on the reference data R . For conventional RDI, the residuals would be: $T_{\text{res}} = T - M(T, R)$. For PI-constrained RDI (PCRDI), the residuals would be $T_{\text{res}} = T - M(T - T_{D,\text{est}}, R)$. In either case, $M(T, R)$ could be a PSF model constructed with a least-squares algorithm like KLIP or with a simple linear combination of reference frames. In this case, we use the latter.

If we instead evaluate $y = [T - T_{D,\text{est}}] - M(T - T_{D,\text{est}}, R)$ (i.e. subtracting the same PSF-model from the disk-subtracted target data), then the result is indicative of how well our estimate of the disk matched the true disk signal in the data -- being positive where we underestimated the true signal, and negative where we overestimated it. PCRDI can be optimized by seeking the values of ($a, b, c, s, \text{incl}, \text{PA}$) such that Σy^2 is minimized. We perform the optimization y over a region excluding and thus unbiased by AB Aur b.

Supplementary Figure 8 below compares our best-fit estimate the protoplanetary disk scattered light-- the polarized intensity divided by the best fit *diskmap* fractional

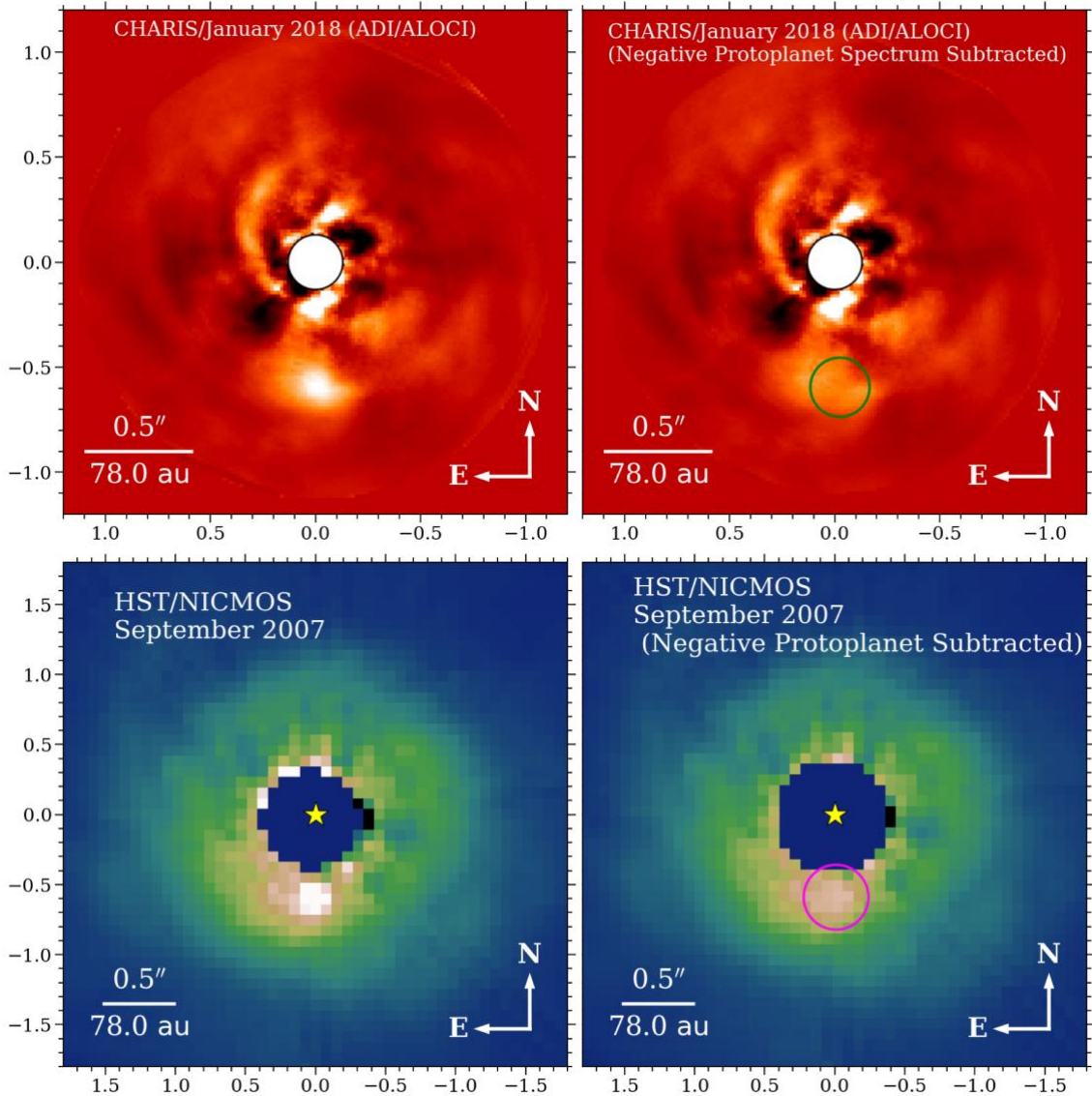
polarization – to the PCRDI-reduced total intensity image and the residuals within our training zone, y . The disk scattered light lacks the pronounced peak seen in the total intensity data that corresponds to AB aur b.



Supplementary Figure 8 – Demonstration that AB Aur b is not a disk feature using PCRDI. (Left) CHARIS PI divided by the optimized diskmap fractional polarization estimate. This is the estimate of total intensity used to improve RDI in PCRDI. (Center) CHARIS optimized PCRDI result. (Right) The objective function for optimized PCRDI, i.e., $y = [T-TD,est] - M(T-TD,est, R)$, which has been derotated and averaged over the sequence. Within the region considered, the total intensity estimate results in a final product that is effectively nulled. All images have been averaged over wavelengths and multiplied by the stellocentric separation assuming the best fitting diskmap scattering surface.

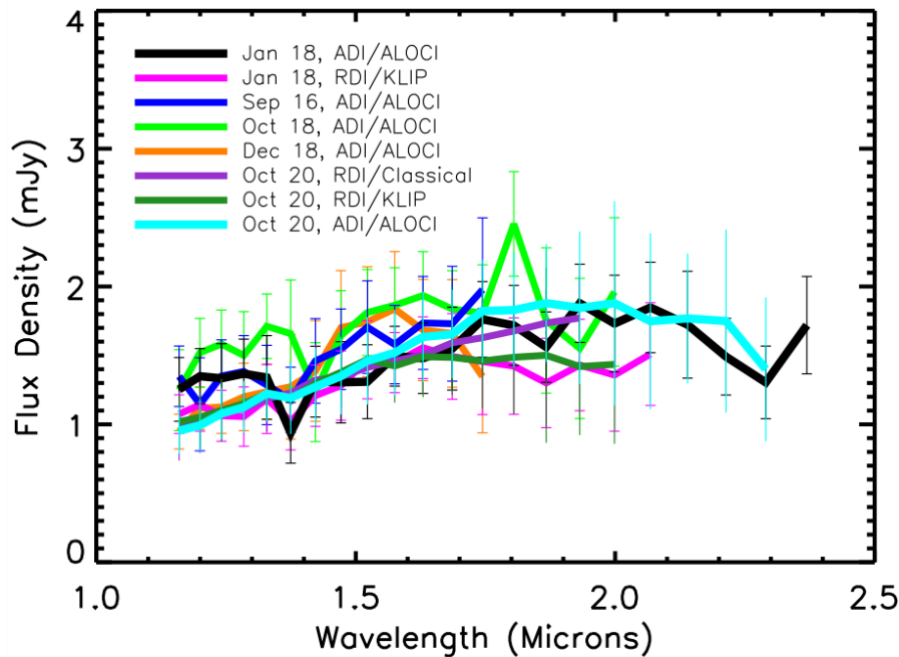
In summary, forward-modeling analyses of CHARIS and HiCIAO data rules out the possibility that AB Aur b is a disk feature artificially made to look like a concentrated source due to aggressive processing. Separately, the detection of AB Aur b using simple classical reference star PSF subtraction in STIS and NICMOS and polarimetry-constrained classical PSF subtraction with CHARIS supports the interpretation that AB Aur b is not a disk feature.

To assess the accuracy of our spectra, photometry, and estimated morphology of AB Aur b, we inserted a negative copy of our synthetic AB Aur b signal used in forward-modeling with a spectrum equal to that we extract from our real data (Supplementary Figure 9). As shown in Supplementary Figure 9 (top-right panel), this negative spectrum nulls the real AB Aur b signal, leaving a flat background. The bottom-right panel of Supplementary Figure 9 shows our HST/NICMOS image with the scaled, synthetic AB Aur b PSF removed. Here too, the residual image shows a flat background at the position of AB Aur b. Removing a PSF from the STIS data shows the same results.



Supplementary Figure 9 – Negative subtraction of AB Aur b. (top panels) CHARIS ADI-reduced image of AB Aur compared to the same image where a negative copy of AB Aur b's spectrum with our assumed morphology is imputed into the observing sequence. (bottom panels) HST/NICMOS F110W PSF subtracted image compared to the same image with the model PSF for AB Aur b removed. In both cases, subtraction of the model protoplanet emission yields a flattened featureless background.

Absolute calibration of the CHARIS data draw from IRTF/SpeX data (PI M. Sitko). The SpeX data cover 0.8 to 5 microns: the measured flux densities agree with values for the optical spectrum. Multiple epochs of SpeX data for AB Aur show at most 10% variability in luminosity and no evidence for variability in the *shape* of the near-IR spectrum that could impact our results.

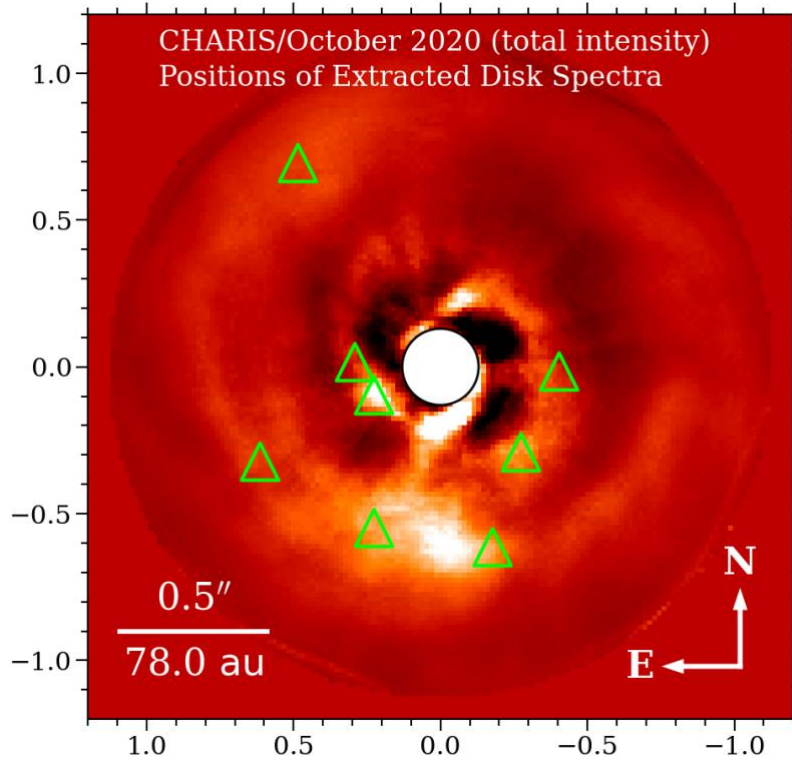


Supplementary Figure 10 – Spectra extracted for AB Aur b from different epochs and with different PSF subtraction algorithms. The wavelength range covers only those channels where we can confidently claim a detection. The shapes of the spectra show excellent agreement across the J and H bands. Error bars denote 1-sigma uncertainties.

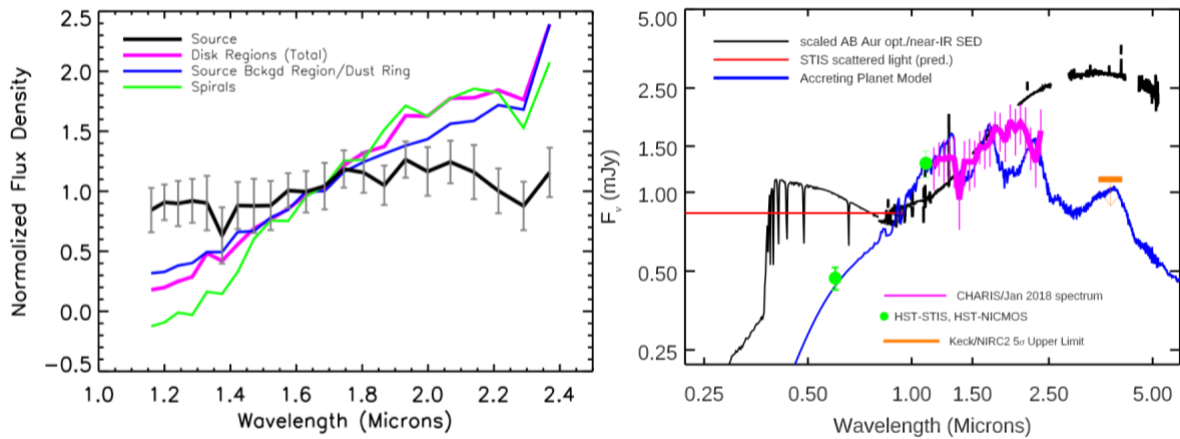
The spectrum extracted for AB Aur b is consistent across epochs, within errors. As shown in Supplementary Figure 10, in the J and H passbands where AB Aur b’s detection is unambiguous, reductions using ADI and RDI, ALOCI and KLIP, yield consistent spectrophotometry. In Ks band, AB Aur b is generally not detected in the poorer quality September 2016, October 2018, and December 2018 data sets. However, spectrophotometry for the higher quality data agree very well within errors, regardless of reduction approach. Similarly, STIS photometry separately reduced from January and February 2021 agrees to within errors.

To assess whether AB Aur b can be explained by scattered starlight, we compare its spectrum with that from the protoplanetary disk extracted from multiple locations (Supplementary Figure 11). Regions include disk locations at position angles flanking AB Aur b, disk locations at comparable angular separations but very different position angles, and extractions along the two spiral arms at smaller separations. In all cases, AB Aur b’s spectrum differs. Supplementary Figure 12 (left panel) compares the normalized AB Aur b spectrum extracted from data processed with ADI/A-LOCI and the AB Aur protoplanetary disk processed with RDI/KLIP (both from January 2018 data). AB Aur b is substantially bluer than the AB Aur protoplanetary disk. Supplementary Figure 12 (right panel) shows the spectral energy distribution comparisons described in the main text. The accreting planet model includes contributions from a planet atmosphere and from magnetospheric accretion (see main text and Methods). As noted in the main text, a simple blackbody with a temperature comparable to that from the planet atmosphere model reproduces AB Aur b’s IR photometry as well. The dissimilarity between the spectra of AB Aur b and the disk

holds for different reduction approaches; each region of the disk for which we extracted spectra is redder than AB Aur b (Supplementary Figure 13).

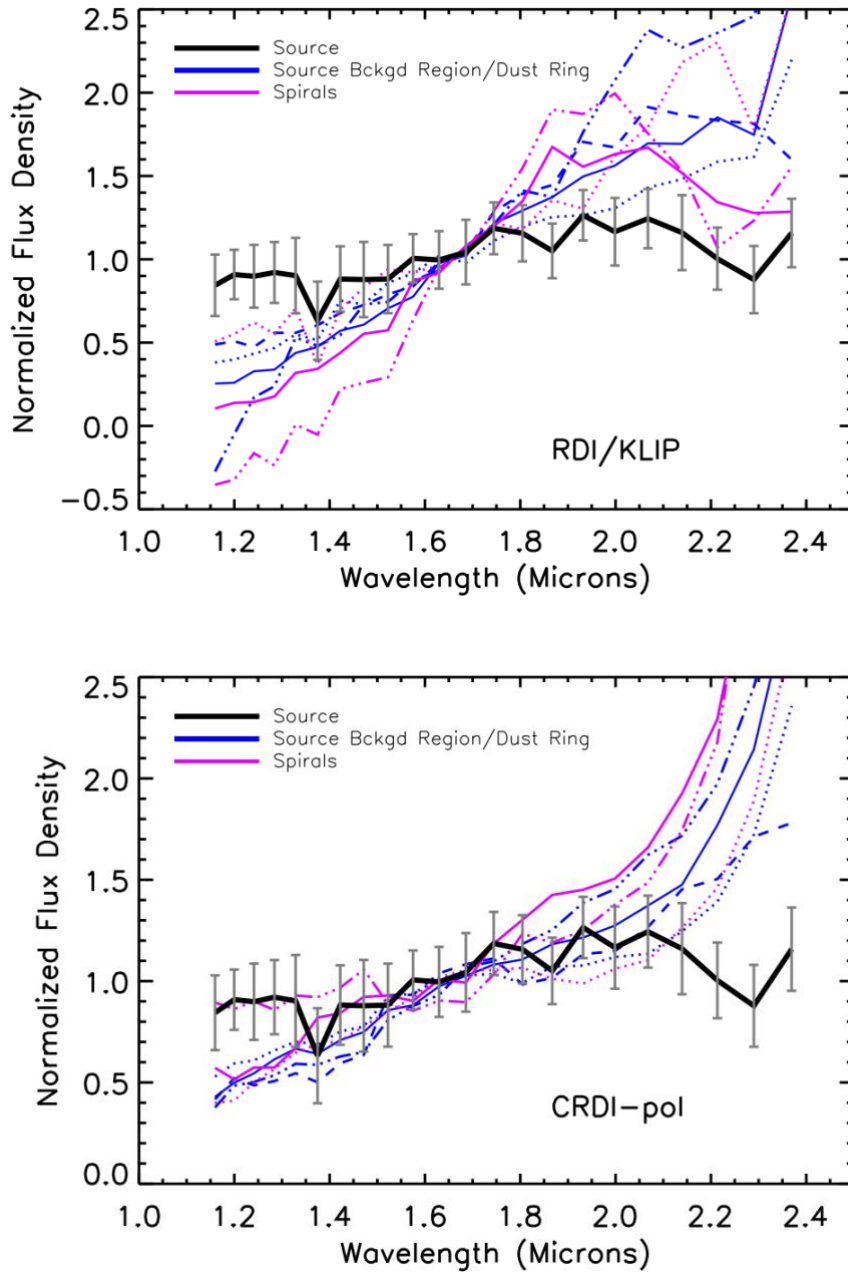


Supplementary Figure 11– Locations of disk spectra extracted in Supplementary Figure 12 denoted by lime-green triangles.



Supplementary Figure 12 –SED modelling of AB Aur b. (left) Normalized CHARIS spectrum of AB Aur compared to extracted spectra of different regions of the AB Aur disk. The AB Aur b spectrum derives from our ADI-ALOCI reduction of the January 2018 data; the disk spectra derive from the RDI-KLIP reduction of the same data. spectra extracted from individual locations and with different reductions show the same trends. (right) AB Aur data compared to a scaled spectrum of the primary and an accreting planet model. The model assumes a temperature of 2200K, gravity of $\log(g) = 3.5$, and radius of 2.75 jovian radii. Magnetospheric accretion is truncated at 7.5 jovian radii; the planet mass is 9 jovian masses and accretion rate is $\dot{M} \sim 1.1 \times 10^{-6} \text{ M}_J/\text{yr}$. Other combinations of planet mass and accretion rate yielding $M\dot{M} \sim 1.1 \times 10^{-5} \text{ M}_J^2/\text{yr}$ likewise can reproduce AB Aur b's SED; a more blackbody-like, featureless

spectrum matched to the near-IR data combined with magnetospheric accretion achieves comparable fits. Analysis in S5 considers the VAMPIRES $H\alpha$ and optical continuum detections. Error bars denote 1-sigma uncertainties.



Supplementary Figure 13 –Spectrum of AB Aur b compared to disk spectra extracted from locations depicted in Supplementary Figure 11. The top panel shows our nominal comparison using RDI/KLIP-reduced data: the average of measurements for the dust ring and spirals is shown in Supplementary Figure 12, left panel. The bottom panel shows similar comparisons for data reduced using polarimetry-constrained RDI, which has poorer speckle suppression at small angular separations but higher throughput than the RDI/KLIP reduction. In both cases, the disk is redder than AB Aur b.

S3. Astrometry of AB Aur b

Precise astrometry of AB Aur b first requires accurate absolute calibration of the ground-based instruments used for detection. The HST instrument astrometric calibrations are exceptionally robust: e.g. NICMOS's pixel scale and north position angle have a precision of 6×10^{-3} mas and 2×10^{-3} degrees, respectively, with a geometric distortion corrected to 0.18 pixels over the full detector⁸. The narrow field NIRC2 camera is precisely calibrated with a pixel scale and north PA offset of 9.971 mas/pixel and 0.262° with exceptionally small uncertainties of 4×10^{-3} mas and 0.02° , respectively⁹.

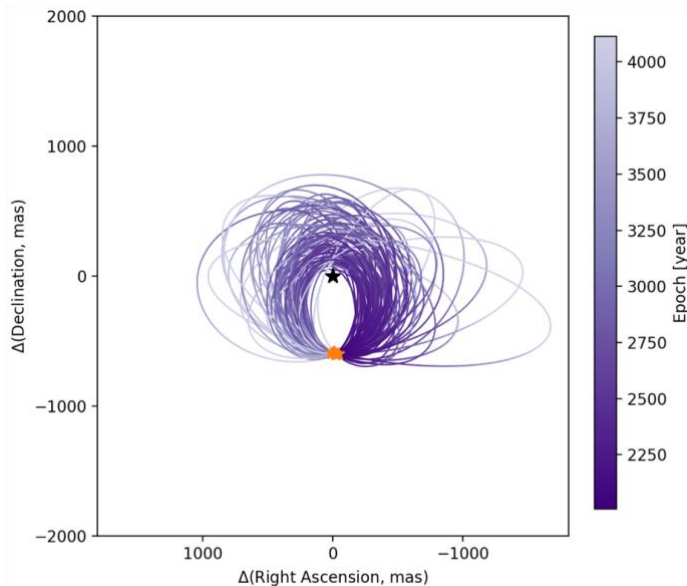
Following our previous, preliminary analysis⁶, we tie astrometric calibration of CHARIS to NIRC2 through epoch-matched observations of HD 1160 to obtain astrometry of the low-mass companion HD 1160 B. As a secondary astrometric calibration for CHARIS, we observed the M5 globular cluster, which has also been observed with HST/WFC3. For HiCIAO, we compared data for DH Tau and kappa And to NIRC2 obtained in December 2015/November 2016 and May 2016, respectively. We used astrometry of their companions to pin HiCIAO's pixel scale and north PA to NIRC2's.

CHARIS, HiCIAO, and NIRC2 data were processed following methods used for AB Aur. We used the IDL function `cntrd.pro` to estimate the centroid position of HD 1160 B, DH Tau B, kappa And b, and stars surrounding our M5 field. These analyses point to a slightly revised CHARIS pixel scale of 16.15 ± 0.05 mas/pixel but the same north position angle offset as derived before: $2.20^\circ \pm 0.27^\circ$. We find no evidence for substantial differences in the north PA offset in CHARIS from epoch to epoch. For HiCIAO, we find a pixel scale and north position angle of $\sim 8.3 \pm 0.1$ mas/pixel and $-1.0^\circ \pm 0.1$. At the separation of AB Aur b, these pixel scale and north PA uncertainties translate into positional uncertainties on the order of 3 mas: uncertainties due to the intrinsic SNR of the detection dominate over these systematic calibration uncertainties.

AB Aur b's computed position slightly varies with our initial guess for the position, typically ~ 0.1 – 0.3 pixels in both coordinates. Therefore, to derive robust astrometry for AB Aur b from ground-based data and estimate conservative errors, we constructed a grid of initial estimates of 4×4 pixels in size bracketing the apparent position and quantitatively determined the final centroid position and its uncertainty from the average and standard deviation of individual estimates drawn from background-subtracted images, weighted by the SNR at each estimated position. Since AB Aur b is not unambiguously detected in all spectral channels for every data set, we focused only on the channels with unambiguous detections. E.g. we included all channels for the 2018 January 06 and 2020 October 02 data but channels 1-15, 1-14, and 1-16 for the 2016 September 18, 2018 October 16, and 2018 December 21 data. To consider the north position angle uncertainty for CHARIS, we also included an astrometric uncertainty of 3 mas. Final errors include this centroid uncertainty estimate, the intrinsic SNR, and absolute calibration uncertainties for CHARIS and HiCIAO.

Table 1 in the main article describes the mean and 68% confidence intervals for AB Aur b’s semimajor axis, eccentricity, and inclination for orbit fitting without restrictions on parameters. Supplementary Figure 14 shown below plots the 100 best-fitting orbits.

Having formed from a protoplanetary disk, AB Aur b may be coplanar with the disk. We therefore investigated a second set of fits adopting a Gaussian prior on the inclination centered on 25 degrees (+/- ~9 degrees). For this fit, the mean of posterior for the semimajor axis lies at ~94.19 au [80.22,108.14]; the eccentricity is a slightly lower 0.2 [0.08,0.32] while the inclination reflects the input prior. Other orbital parameters (e.g. longitude of the ascending node) remain poorly constrained.

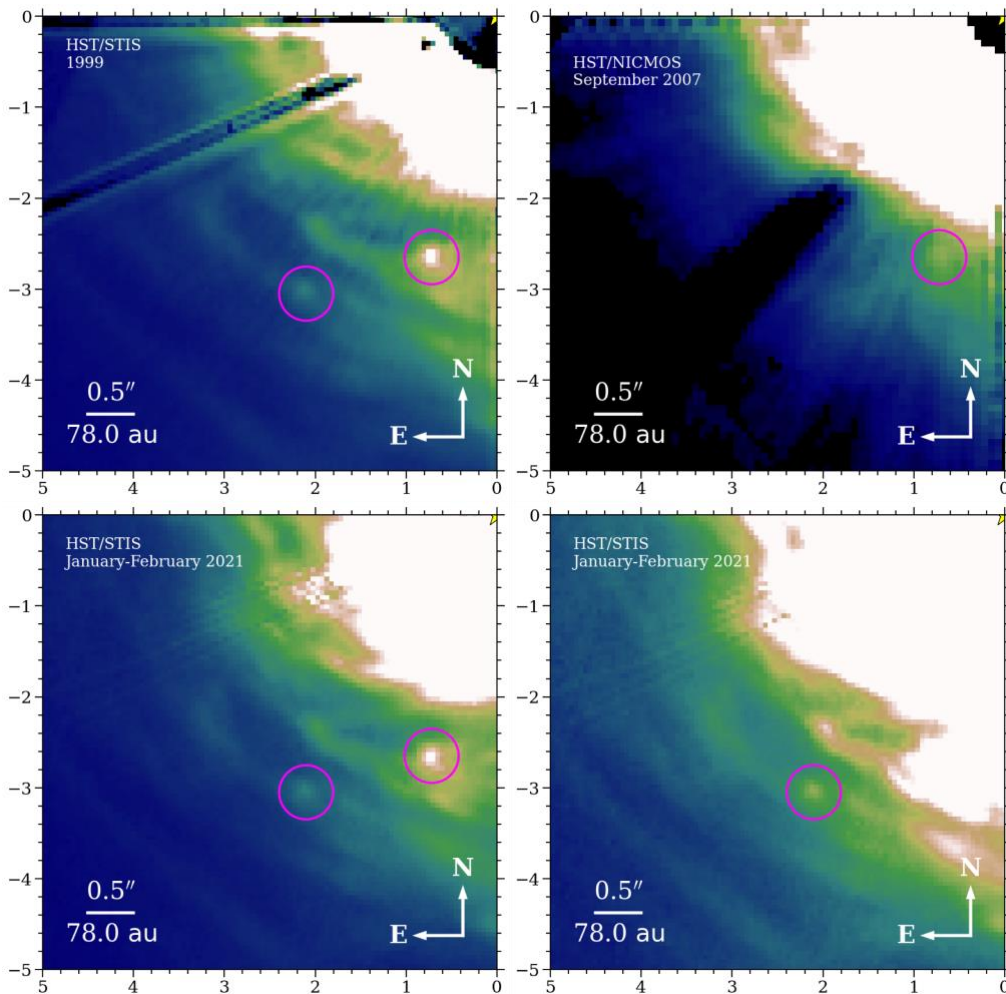


Supplementary Figure 14 – The 100 best-fitting orbits for AB Aur b from our astrometric analysis. Most solutions have AB Aur b near aphelion.

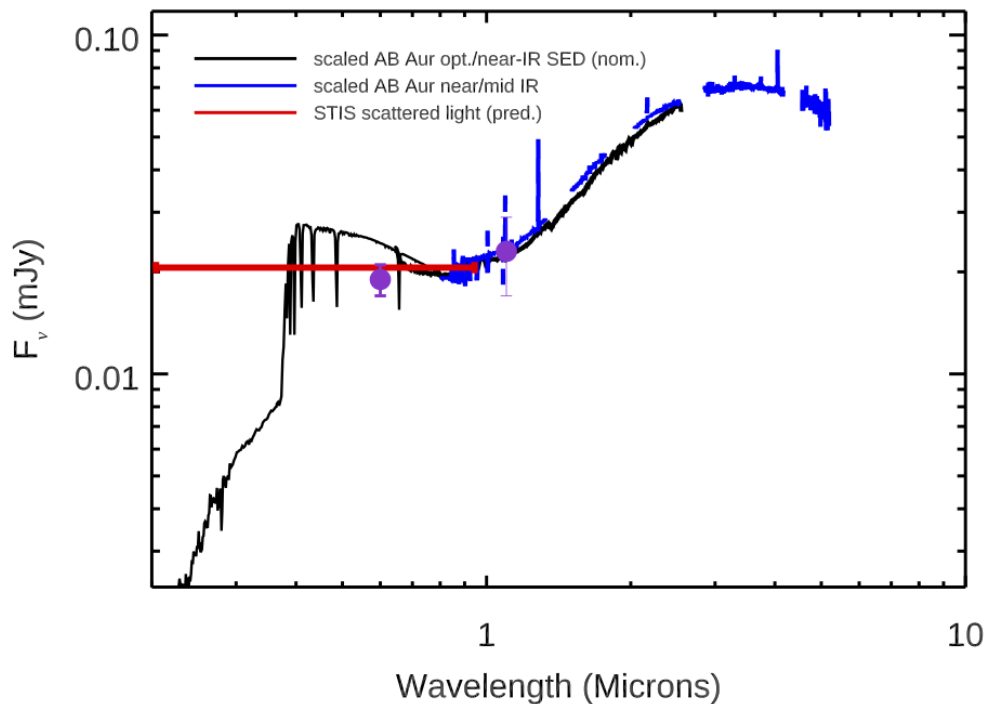
S4. Wider-Separation Clump-like Signals

As described in the main text, HST data identify at least one, possibly two concentrated emission clumps at extremely large angular separations of $\rho \sim 2.75''$ and $3.72''$ (429 au and 580 au): hereafter, sources “c” and “d”. Supplementary Figure 15 displays these sources in the 1999 and 2021 STIS data (left, middle) and 2007 NICMOS data (right). In the STIS data, both sources are detected, with SNRs of 9–12 for “c” and 6–9 for “d”. Only source “c” is visible in NICMOS data (SNR ~3). While we detect no other similar sources in the AB Aur disk, much of the north half of the AB Aur disk is blocked by the coronagraph in our most sensitive HST data set (2021 STIS data).

Following similar analysis for AB Aur b, we estimated the size of these two point-like features. Their radii are roughly $\sim 0.063''$ — $0.079''$ in size. Using the same methods adopted for AB Aur b, we measure STIS photometry of 20.40 ± 0.11 and 22.48 ± 0.15 magnitudes for “c” and “d”, respectively. These two features at wider separation are not detected in polarimetry, although neither is the disk at such wide angular separations detected. These two features have STIS and NICMOS photometric measurements that can conceivably be matched by a scattered starlight (Supplementary Figure 16). Thus, they remain *candidate* sites of planet formation requiring further study.



Supplementary Figure 15 – Detection of two additional clump-like signals at ultra-wide separations in AB Aur’s disk. (top-left) HST/STIS data from 1999 showing the detection of sources ‘c’ and ‘d’ (brighter and dimmer source, respectively) at $\sim 2.75''$ and $\sim 3.72''$ and (top-right) HST/NICMOS data from 2007 showing a marginal detection of source ‘c’. (bottom-left) Detection of source ‘c’ and ‘d’ in 2021 STIS data: the left panel is at a similar color stretch to that displayed for the 1999 STIS data.. The right panel has a more aggressive color stretch to more clearly show source ‘d’.



Supplementary Figure 16 – Analysis of source ‘c’. Photometry of source c (purple dots) compared to the spectrum of AB Aur. Error bars denote 1-sigma uncertainties.

S5. Details on Modeling AB Aur b’s Optical Emission from VAMPIRES: Evidence for Accretion?

Supplementary Figure 12 (right panel) shows that the STIS, NICMOS, CHARIS, and NIRC2 data are inconsistent with a stellar photosphere + sub-au dust component expected for disk feature unrelated to a planet. For presentation clarity, we omitted comparisons to ground-based optical photometry from VAMPIRES. Here, we consider the VAMPIRES measurements in more detail.

AB Aur b’s flux density in $H\alpha$ is nearly a factor of 3 higher than its continuum brightness (3.01 mJy vs 1.13 mJy or a factor of ~ 2.66). Normally, this high $H\alpha$ would be unambiguously interpreted as protoplanet accretion. However, AB Aur itself has strong $H\alpha$ from accretion: its line flux density is a ~ 2.4 higher than the continuum. As the $H\alpha$ detections themselves are only at SNR ~ 5 – 6 , it is not possible to definitively tell whether $H\alpha$ is due to scattered starlight or accretion. Subtracting the continuum image from the $H\alpha$ image removes all of the protoplanetary disk scattered light on the differenced image (e.g. the spirals) but leaves residual emission at the $\sim 2\text{-}\sigma$ level at the approximate position of AB Aur b. Another challenge with interpretation is that VAMPIRES’s astrometric calibration is still a work in progress: it is not clear whether VAMPIRES signal is entirely coincident with AB Aur b or is displaced in azimuth. Thus, we consider the VAMPIRES to be *consistent with* optical emission from AB Aur b but not strictly conclusive as is the case for CHARIS, STIS, and NICMOS data.

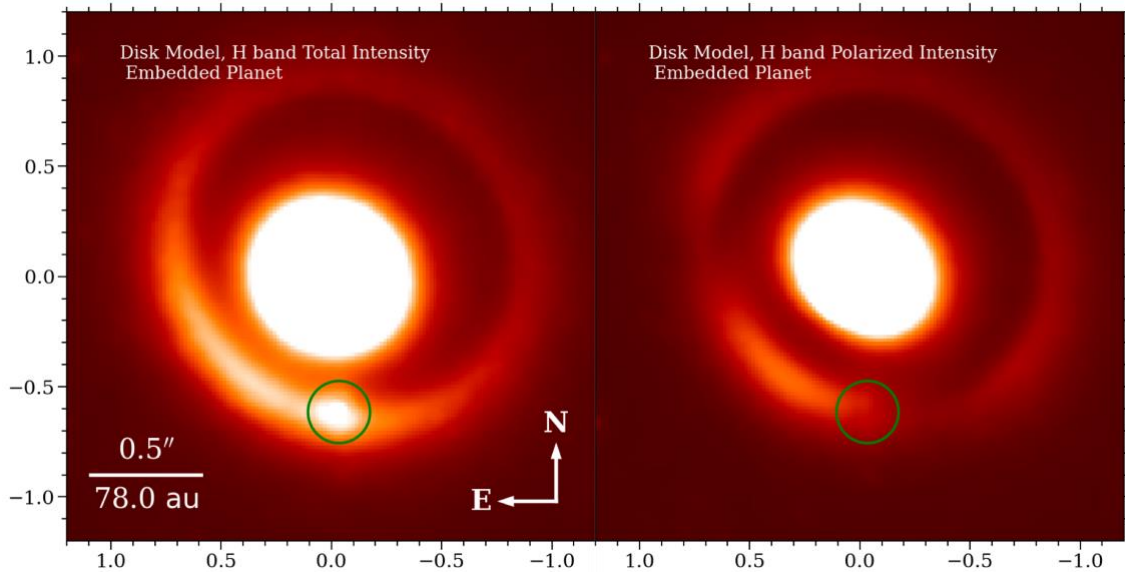
Future, deeper observations with VAMPIRES or higher-resolution spectra from other facilities (e.g. VLT/MUSE) may clarify whether this emission results from accretion or a scattered light component.

S6. Synthetic Scattered Light Images of AB Aur: An Embedded Protoplanet Model

We used the following approach to set up a Monte Carlo Radiative Transfer model of an embedded protoplanet in MCMaX3D to reproduce the appearance of AB Aur b. The model adopts a temperature of 9770K and luminosity of 59 solar luminosities for the primary and an optical extinction of $A_V = 0.5$ and a distance of 155.9 pc for the system. Scattered light imaging reveals the protoplanetary disk down to an inner working angle of $0.1''$ (~ 16 au) and exterior to ~ 600 au, where the majority of this light is within 300 au¹⁰. Millimeter imaging reveals emission concentrated near the star and in a ring approximately $0.75''$ — $1.5''$ from the star (see main text). Thus, we considered two separate dust components: a population of small grains extending from the inner disk boundary out to 300 au and a more massive population of dust grains confined in a ring from 130 au to 250 au.

We varied properties of each dust population to simultaneously reproduce the surface brightness of AB Aur's disk in scattered light, its millimeter emission, and its spectral energy distribution. This parameter search led to the following values. For the first dust component, we set the inner edge of the disk to 0.27 au, similar to the 0.24 au value found from interferometric modelling¹, but with a rounded disk wall where the peak density is not reached until 0.5 au. The disk is flared with a scale height varying as $r^{1.3}$ with a shallow surface density power law of $r^{-0.5}$. Dust grains range from $0.1 \mu\text{m}$ to $1 \mu\text{m}$, with a standard $\beta = -3.5$ power law size distribution, and a total dust mass of 1.75×10^{-5} solar masses. For the second dust component, we set the inner edge of the disk to 130 au, similar to the deprojected radius of much of the disk seen in scattered light, again with a rounded disk wall where the peak density is not reached until 160 au. The disk is flared with the same scale height power law but has a steeper surface density power law of $r^{-1.0}$. Dust grains range from $1 \mu\text{m}$ to $100 \mu\text{m}$, again with a standard $\beta = -3.5$ power law size distribution, and a total dust mass of 1.25×10^{-4} solar masses. For both dust populations, we assume carbon-less grains with a 0.2 fractional porosity.

To generate a detailed model of the disk temperature structure and optical depth we used a Monte Carlo simulation with 10^7 photons. Generating synthetic scattered light images used 5×10^7 photons, although we saw no discernable difference in the images after 10^7 photons. Synthetic millimeter images required a comparable number of photons. While the disk model overpredicts the scattered light brightness at small ($<0.3''$) separations, it accurately reproduces the surface brightness of the disk in H band at wider, $>0.4''$ separations and reproduces the geometry of the dust ring seen in the millimeter.



Supplementary Figure 17 – Comparison between synthetic total and polarized intensity scattered light images for an embedded AB Aur b. (left) Synthetic image of AB Aur, its protoplanetary disk, and an embedded AB Aur b at 1.63 microns in total intensity. (right) The same model in polarized intensity.

We estimated the optical depth along our line of sight at locations similar to AB Aur b by comparing its emission in absence of a disk to its emission embedded in a disk. At the companion’s location, the disk is marginally optically thin/thick. The model shown in Figure 5 in the main text has an optical depth at AB Aur b’s location of $\tau \sim 1.3$ in H band along our line of sight, although models with slight parameter variations of $\tau = 0.25\text{---}2$ also reproduce the scattered light brightness of the disk. In these conditions, AB Aur b emits light which is scattered off nearby dust grains, elevating the surface brightness of the image over a radius of $\sim 0.05''$ in the simulated image. When convolved with the CHARIS PSF, AB Aur b appears spatially extended, with a FWHM of $\sim 0.1''$, similar to the measured size of the companion in CHARIS. The signal from AB Aur b over this larger area is roughly equal to its point-source emission in absence of any intervening protoplanetary disk material. For models with progressively higher optical depths ($\tau \gg 10$), the near-IR emission becomes extremely diffuse with less measurable signal and eventually invisible. Similarly, for our nominal model the emission at optical wavelengths is more diffuse.

While this model is meant purely as a proof of concept and not a detailed, quantitative fit to the data. We further emphasize that this model is agnostic as to the underlying mechanism responsible for a planet being located at wide separations: core accretion or disk instability.

Importantly, however, the model does reproduce key aspects of the CHARIS images. It does predict that AB Aur b should appear extended. While the overall polarization level of the synthetic model is low compared to observations, the synthetic polarized intensity image does not reveal any elevated emission at the position of AB Aur b (Supplementary Figure 17). Critically, the detection of some polarized emission at AB Aur b’s position in the model and in the real data does not mean that AB Aur b

itself is detected in polarized light because AB Aur b is embedded in a disk which should have a polarized light signal. Rather, the lack of concentrated emission at the location of AB Aur b in polarized light implies that it is not detected.

In order to generate an appearance of AB Aur b consistent with our data, the model requires a narrow range of optical depths: marginally optically thin values for the disk optical depth at the protoplanet's position. However, the surface brightness of the disk is consistent with observed CHARIS values. Within the framework of MCMMax3D, the disk model parameters chosen are then those that reproduce the near IR scattered light images irrespective of whether or not there is a planet.

S7. Tying AB Aur Images to Simulations of Planet Formation: A Disk Instability-Produced Clump

Details for how we construct a model of planet formation by disk instability are as follows. We construct a model two-dimensional disk in cylindrical coordinates. We then solve for the vertically integrated equations of motion with self-gravity and finite cooling

$$\begin{aligned}
\frac{D\Sigma}{Dt} &= -\Sigma \nabla \cdot \mathbf{u} \\
\frac{D\mathbf{u}}{Dt} &= -\frac{1}{\Sigma} \nabla P - \nabla \Phi + \frac{1}{\Sigma} \nabla \cdot \boldsymbol{\zeta} \\
T \frac{Ds}{Dt} &= -c_v \frac{(T - T_{\text{ref}})}{\tau} + \Gamma_{\text{sh}} \\
P &= \Sigma c_s^2 / \gamma \\
\Phi &= \Phi_{\text{sg}} - \frac{GM}{r} \\
\nabla^2 \Phi_{\text{sg}} &= 4\pi G \Sigma \delta(z)
\end{aligned}$$

where Σ is the density, \mathbf{u} is the velocity, P is the pressure, Φ is the gravitational potential, $\boldsymbol{\zeta}$ is the shock viscosity tensor, T is the temperature, s is the entropy, c_v is the specific heat at constant volume, T_{ref} is a reference temperature, τ is the thermal time, Γ_{sh} is the shock heating, c_s is the sound speed, γ is the adiabatic index, Φ_{sg} is the disk selfgravity, G is the gravitational constant, M is the stellar mass, and r the stellocentric distance. The advective derivative is

$$\frac{D}{Dt} = \frac{\partial}{\partial t} + \mathbf{u} \cdot \nabla$$

We use the Pencil Code¹¹ to solve the equations of motion. We capture shocks using an explicit shock viscosity prescription. The third term in the momentum equation is the viscosity required to spread shocks out to resolvable width, and the last term in the entropy equation is the shock viscous heating. The shock viscosity tensor takes the form of a bulk viscosity

$$\zeta_{ij} = \nu_{\text{sh}} \Sigma \delta_{ij} \nabla \cdot \mathbf{u}$$

and the associated shock heating is

$$\Gamma_{\text{sh}} = v_{\text{sh}} (\nabla \cdot \mathbf{u})^2$$

They depend on the shock viscosity, which we define numerically as

$$v_{\text{sh}} = c_{\text{sh}} \langle \max_5 [(-\nabla \cdot \mathbf{u})^+] \rangle \min(\Delta x)^2$$

The actual form of the shock viscosity that we use has been described in [12]. The superscript plus sign indicates the positive part of the quantity. The “5” subscript indicates the maximum is taken within 5 grid zones. As long as the shock is resolved, the value of the shock viscosity coefficient does not change the amount of heating; rather, it just changes the volume (number of grid cells) over which the shock energy is spread.

The reference temperature T_{ref} is set to the initial temperature at every radius. Sixth-order hyper-dissipation terms are added to the evolution equations to provide extra dissipation near the grid scale, as discussed in [13]. These terms are needed for numerical stability because the high-order scheme of the Pencil Code has little overall numerical dissipation¹⁴. They are chosen to produce Reynolds numbers of order unity at the grid scale, but then drop as the sixth power of the scale at larger scales, so that they have negligible influence on the large-scale flow.

The disk ranges from 30 to 300 au, and full 2π azimuthal coverage. The resolution is 432 grid cells in radius, and 864 cells in azimuth. The grid is logarithmically spaced in radius, and linear in azimuth.

For boundary conditions, we use sponge zones in the radial boundaries, that drive all quantities back to the initial condition. The width of the sponge is 3 au at the inner boundary and 30 au in the outer boundary. The quantities are driven back to the initial condition within 10^{-2} orbit at 100 au. Boundary condition for radial velocity is zero gradient; azimuthal velocity, density, and entropy use constant gradient.

The density is initially set as an exponentially truncated disk

$$\Sigma = \Sigma_0 \exp \left[- \left(\frac{r}{r_0} \right)^2 \right]$$

with $r_0=100$ au. In the inner disk (30-70 au), this density profile is well approximated by a power-law falling as square root of the radius. The temperature follows a power law

$$T = T_0 \left(\frac{r}{r_0} \right)^{-q}$$

with $q=1$. T_0 is set to 30K at 100 au. The sound speed is given by

$$T = \frac{c_s^2}{c_p(\gamma - 1)}$$

where $c_p = \gamma c_v$ is the specific heat at constant pressure. The specific heats are related to the universal gas constant R by

$$R = \mu(c_p - c_v)$$

where μ is the mean molecular weight of the gas, set to 2.3, for a 5:2 H₂-He mixture. Given $\gamma=1.4$, the sound speed at 100 AU is about 0.33 km/s. This sets the disk scale height $H=c_s/\Omega_K$ (where Ω_K is the Keplerian frequency) at 100 au as 0.07, considering a central mass of $M=2.4$ solar masses.

The reference volume density ρ_0 is 10^{-12} g/cm³, leading to a column density of $\Sigma = 2.7$ g/cm² at 100 au. These physical conditions translate into Toomre Q values

$$Q = \frac{c_s \Omega}{\pi G \Sigma}$$

below 1 between 50 and 150 au.

The initial radial velocity is zero; the initial azimuthal velocity is corrected by the pressure gradient and self-gravity

$$\phi^2 = \Omega_K^2 + \frac{1}{r} \left[\frac{1}{\Sigma} \frac{\partial P}{\partial r} + \frac{\partial \Phi_{sg}}{\partial r} \right]$$

noise added in the velocity field at the $5 \times 10^{-3} c_s$ level. The cooling time is set to $\beta = \Omega \tau = 10$ orbits. The gas self-gravity is solved via fast Fourier transforms in cylindrical coordinates with the method of logarithmic spirals¹⁵. Both the coefficients of shock and hyper diffusivity are set to 20.

The Bonnor-Ebert mass, which gives the collapsing mass for an isothermal sphere in a medium of external pressure p_0 is

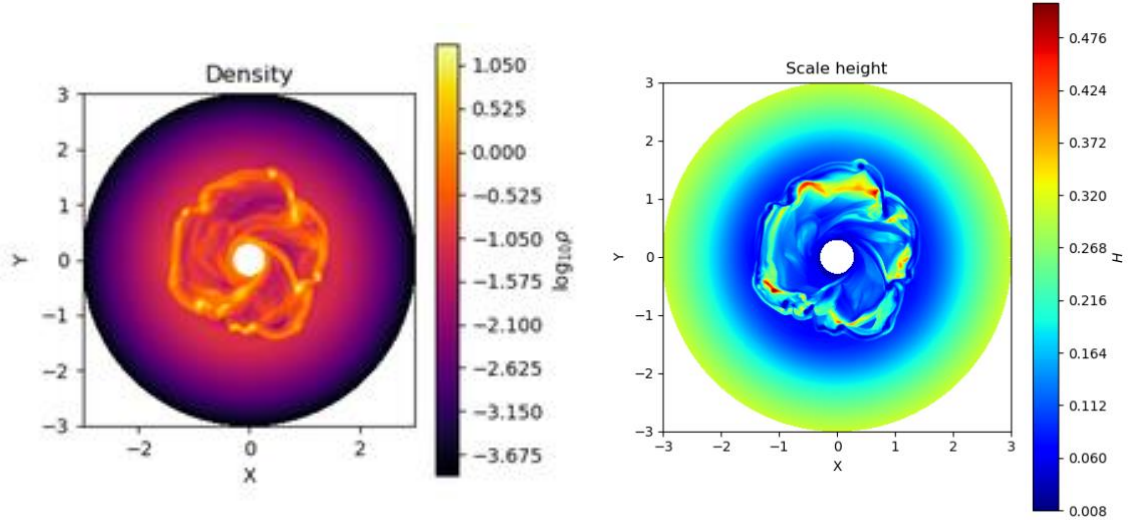
$$M_{BE}(p_0) = \frac{225}{32\sqrt{5}\pi} \frac{c_s^4}{(aG)^{3/2}} \frac{1}{\sqrt{p_0}}$$

where $a=1$ for constant density, and $a=1.67$ for a sphere that is denser in the center. For our choice of parameters ($\rho = 10^{-12}$ g/cm³, $T=30$ K, $\gamma=1.4$), the Bonnor-Ebert mass is 0.93 Jupiter masses, which sets the expectation for the mass of the clumps formed in the model.

Within a few orbits, the disk breaks into fragments (Supplementary Figure 18). The left panels show the gas density, the right panel the local disk scale height considering self-gravity¹⁶

$$H' = \frac{H_{sg}}{2} \left(\frac{H_*}{H_{sg}} \right)^2 \left[\sqrt{1 + 4 \left(\frac{H_{sg}}{H_*} \right)^2} - 1 \right]$$

where $H_{sg} = QH$ and $H_* = (\pi/2)^{1/2}H$. Notice that the location of the clumps corresponds to regions of *low* scale height, evidencing $Q \ll 1$.



Supplementary Figure 18 The state of the disk after 10 orbits. The unit of the axes is 100 au. *Left:* Density is shown in units of 10^{-12} g/cm³. The disk has fragmented into many gravitationally unstable clumps. *Right:* The local scale height. The dark region just counter-clockwise from the scale height peak at the 8 o'clock position, identifies the collapsing clump's position. Other clumps have lower density and are cooler and thus are harder to see in scattered light.

To produce a synthetic image, we perform full radiative transfer post-processing with RADMC-3D¹⁷, a popular Monte Carlo radiative transfer software. RADMC-3D combines a Monte Carlo code with a ray-tracing mode to simulate observations of the resulting temperature distribution. In practice, we first use thermal Monte Carlo simulations to determine the temperature of the optically thin regions of the disk. Then, a ray-tracing computation is used to create a synthetic image of what would be observed at infrared wavelengths of interest. The last snapshot was taken from the hydrodynamical simulation and its parameters were input into RADMC-3D, using the pipeline developed in [18].

Since the hydrodynamical model is 2D, we extend the model in the vertical direction using the scale height shown in Figure 1, and assuming hydrostatic equilibrium

$$\rho = \rho_0 \exp \left[-\frac{z^2}{2H^2} \right]$$

The grid is extended in spherical coordinates, with 128 points in the meridional direction, covering 10 scale heights above and below the midplane.

The central star is 2.5 solar radii, at effective temperature 9770 K. We assume well-coupled micrometer-sized dust grains to be perfectly coupled to the gas. The dust density then follows directly from the Pencil Code output, scaled down by a factor of 100 (the dust-to-gas ratio) and converted into cgs units of grams per cubic centimeter. We use the wavelength-dependent opacities from [19]. The radiative field is sampled with 10^7 photons, out of which are treated as scattering. To reproduce AB Aur b, an extra source of photons is placed at $(X,Y)=(-90,-80)$ au. The radius of the source is set to 2 Jupiter radii, with temperature 5000 K. While some studies find far cooler temperatures associated with GI²⁰⁻²¹, they typically assume an isothermal gas disk or do not include accretion luminosity of the contracting clumps with the central gravitational potential not well resolved. In contrast, other approaches find central clump temperatures of at least 1500K, up to 5000--6000 K²²⁻²⁴.

As with the scattered light model of an embedded planet, this disk instability model is a proof-of-concept and is not intended to be a rigorous approach to precisely reproduce all aspects of the observed IR data. Among its potential weaknesses, the disk instability model produces many clumps, not one, although these clumps are of different densities or at least different locations such that they are not all equally visible. The detectability of only one may require unique conditions in the disk and/or viewing geometry effects.

Nevertheless, the model does capture key properties of our IR images. Namely, it produces a bright clump-like signal at $\sim 10^{-4}$ contrast at an angular separation of $0.6''$ (~ 115 au, deprojected): consistent with our data. Furthermore, it produces spiral density waves, where the signal we interpret as AB Aur b lies at the terminus: consistent with the modeling of spirals seen in ALMA data.

Taking together these simulations and the observed system properties lends strong credibility to the view that AB Aur b is protoplanet being formed by disk instability. Other recent work likewise identifies the AB Aur system as a potential site for planet formation by disk instability²⁵, although they focus on features possibly interpreted as planets at smaller separations based on VLT/SPHERE results (see next Section).

Regardless of the details of AB Aur b's exact formation history, AB Aur b identifies evidence for a planet formation on wide separations and the system shows clear signs of having gravitationally unstable disk, which likely influence its formation. Future observations from the ground and space as well as future, sophisticated numerical simulations may clarify which interpretation is better explains the system.

S8. The Emission Source for AB Aur b: Planet Atmosphere, Circumplanetary Material, or Both?

While analysis in S2 shows that AB Aur b is not scattered starlight misinterpreted as a protoplanet, pinpointing the object's emission source is challenging. The CHARIS and NICMOS infrared detections and NIRC2 upper limits are consistent with thermal emission in the ~ 2200 K range. However, emission this cold cannot explain the STIS photometry. Thus, in S2 we considered a composite model, consisting of a ~ 2200 K planet atmosphere to fit the IR data and a much hotter component tracing magnetospheric

accretion to fit our optical data. We emphasize, though, that this fit is not unique: i.e. just because the planet atmosphere model reproduces the shape of the IR spectrum, it does not follow that we *must* be seeing the photosphere of a planetary-sized object. Blackbody emission of a comparable temperature – such as one might expect from a circumplanetary material --likewise can reproduce AB Aur b’s IR spectrum.

Thus, AB Aur b’s emission is consistent with two possibilities: 1) emission solely from circumplanetary material (i.e. a circumplanetary disk or envelope) or 2) emission from a ~2200 K planetary atmosphere with a roughly Jupiter size scale *and* a hotter circumplanetary component. The data themselves do not yet allow us to easily distinguish between these two scenarios. However, Scenario 1) is likely favored because embedded protoplanets are expected to be surrounded by either flattened circumplanetary disks or spheroidal circumplanetary envelopes, both of which are fractions of a Hill sphere in size and obscure any nascent planet atmosphere²⁶. The hot emission component would likely originate from the shockfront of a circumplanetary disk/envelope instead of a planet atmosphere. For a roughly spherical circumplanetary envelope, radiative transfer resembles that of a stellar atmosphere. Photons from the embedded planet are successively absorbed, scattered, and re-emitted until they escape. The envelope/disk could contain well mixed dust grains whose small, micron-to-submicron sizes resemble those typical of protoplanetary disks. In such a case, the emission spectrum would be relatively featureless, lacking the sawtooth-like IR spectrum shaped by water, methane, and carbon monoxide opacity as expected for a ~2200 K photosphere²⁷.

Follow-up data spanning a wider range of wavelengths may clarify AB Aur b’s emission source(s). If some of AB Aur b’s IR emission originates from a planetary atmosphere, higher resolution and higher quality data may reveal expected molecular absorption. Better sampled red optical photometry may constrain the temperature of the hot emission component. AB Aur b’s non-detection at Lp strongly disfavors at least some models of an extended, accreting circumplanetary disk that intercepts and reprocessed emission²². However, a future mid IR detection of AB Aur b drawn from higher-quality data may provide evidence of cooler circumplanetary disk emission and motivate new models of circumplanetary disks, circumplanetary envelopes, and/or accretion-driven luminosity.

S9. Comparison with VLT/SPHERE Near-Infrared Results from Boccaletti et al. (2020) and Other Recent Work

As described in S1, we recover AB Aur b through an independent reduction of VLT/SPHERE total intensity data first published in [28]. The authors graciously allowed us to visually inspect their total intensity reduction. Modest field rotation does cause the ADI-reduced total intensity data to be heavily self-subtracted. However, upon a joint reinspection with the authors, AB Aur b is visible in their data for extremely conservative reductions, albeit attenuated by processing (A. Boccaletti, pvt. comm.), consistent with our detections. Greater field rotation and the ability to use a reference star for PSF subtraction allowed us analyze the same system from CHARIS data in a way that is less affected by algorithmic biasing.

The SPHERE paper identified other structures in the AB Aur disk potentially connected to planet formation. In addition to resolving spiral structure down to $\sim 0.1''$, the study identified other structures in the disk possibly connected to planets that are not the focus of this work. Specifically, they identified a twist in one of the spiral arms at $\rho \sim 0.16''$ at a position angle of $\sim 203.9^\circ$ (“f1”) and a point-like clump at $\rho \sim 0.68''$, 7.8° qualitatively similar to sources c and d in this work.

We easily resolve the inner spirals in most CHARIS data sets; the high-quality January 2018 and October 2020 data processed using reference star subtraction provide a particularly clear view of this region minimally biased by processing. Inspecting the region at the “f1” position does not unambiguously reveal a point source although it may identify a local brightness maximum in the spiral. Between the two data sets, the intensity of the spiral region at “f1” is the same to within 20%, in contrast to the order of magnitude difference identified by Boccaletti et al. and attributed to signal-loss from ADI. We do not find clear evidence yet that the spiral related to “f1” is rotating counterclockwise, although a longer time baseline and PDI data more amenable to removing the stellar halo may reveal such motion.

While our work was under final review, a Large Binocular Telescope-led (LBT) group posted preprints for two studies – Betti et al. [29] and Jorquera et al. [30] -- using 2–4 μm imaging to assess properties of the AB Aur disk and identify any companions. Over this wavelength range, they found that AB Aur’s disk has a very red scattered-light disk color. They do not identify any companions, focusing their analyses on the non-detection of candidate sources identified from SPHERE polarimetry.

Visual inspection shows that our SCEXAO/CHARIS data yields a far sharper view of the AB Aur system than the LBT data sets and thus should be viewed as authoritative over the latter. The LBT team does not detect spirals in their shortest wavelength (Ks band) data, attributing the non-detection to optical depth effects or variability. In comparison, the spirals are detected in every SCEXAO/CHARIS and HiCIAO dataset shown in Figure S1, obtained over the course of 2 years (e.g. see Figure S3, right panels). Our data’s advantages are likely due to the higher-order adaptive optics correction enabled by SCEXAO coupled with more high-contrast imaging friendly seeing experienced on Maunakea. We also note that our detection is at lowest contrast with the disk at Ks: imaging AB Aur b at longer wavelengths will be even more challenging.

Both our Keck/NIRC2 Lp data and the LBT Lp data resolve the ring and detect the inner spirals but do not detect AB Aur b. The LBT data report contrast limits by calculating pixel-to-pixel noise maps from the standard deviation of values within a sliding box of $1.5 \lambda/D$. The noise map for a point source covering many pixels, though, should be calculated from the robust standard deviation of pixels in a convolved image (e.g. convolved with a top-hat filter sized to a point source or instrumental PSF), which is typically far larger than the per-pixel standard deviation. Detection limits for an extended source like AB Aur b will also be different from that of a point source. Future imaging with facilities like the upgraded Keck/NIRC2 or JWST will improve upon our limits for AB Aur b’s emission in the thermal IR.

The spiral structure within 1 arcsecond of AB Aur and the morphology of the disk at wider separations will be the subject of future CHARIS and HST studies.

S10. AB Aur in the Context of other Directly Imaged Protoplanetary Systems

AB Aur now joins PDS 70 as a system with directly-imaged protoplanets. Like AB Aur b, PDS 70 bc show orbital motion, near IR photometry inconsistent with scattered light from the star, and a low polarization consistent with its emission originating from a planet, not a pure disk feature²⁹. AB Aur b and PDS 70 bc also show H α emission⁴, although AB Aur b's detection may have origins other than accretion. In contrast to PDS 70 bc, though, AB Aur probes embedded planet formation at ~ 100 au around massive stars, not the protoplanets lying within a cleared disk and orbiting on far smaller, solar system scales around stars less massive than the Sun. Thus, the two systems are laboratories for understanding planet formation on different scales, at evolutionary states, around different kinds of stars, and likely due to different formation mechanisms.

Other systems may harbour candidate protoplanets. For instance, two studies presented detections of protoplanets around the young, Sun-like star LkCa 15 from sparse aperture masking interferometry (SAM) and H α differential imaging³⁰⁻³¹. However, later observations showed that the SAM detections correspond to disk features³² and the H α emission may also originate from the disk³³. Being a young, solar-mass star with candidate companions at ~ 20 au, the system also bears more of a resemblance to PDS 70 than to AB Aur.

HD 100546 is a 2 solar-mass star with one protoplanet candidate at ~ 50 au (HD 100546 b) and another at ~ 13 au (HD 100546 c), just interior to the gap in the protoplanetary disk³⁴⁻³⁶. The system is more similar to AB Aur than PDS 70 or LkCa 15. However, the nature of the candidates remains tentative. Ambiguities in the astrometry and spectra of HD 100546 b complicate its interpretation³⁷. HD 100546 c is thus far reported in a single epoch in the peer-reviewed literature: follow-up in the near term may be precluded if the candidate is passing behind the disk wall³⁸. Similarly, several studies report the detection of candidate companions around MWC 758 in the thermal IR: one on a solar system scale and one at a wide separation at the terminus of a spiral arm³⁹⁻⁴⁰. However, follow-up observations have yet to confirm these companions to establish orbital motion and clearly distinguish them from disk features⁴⁰⁻⁴¹. Lacking the orbital motion, disambiguation from protoplanetary disk scattered light, and spectral confirmation obtained with AB Aur b, HD 100546 bc and MWC 758 bc remain candidates requiring further study and confirmation.

References

1. Tannirkulam, A., Monnier, J., Harries, T. J., A Tale of Two Herbig Ae Stars, MWC 275 and AB Aurigae: Comprehensive Models for Spectral Energy Distribution and Interferometry, *Astrophys. J.*, 689, 513-531 (2008)

2. Prugniel, Ph., Soubiran, C., A database of high and medium-resolutions stellar spectra, *Astron. Astrophys.*, 369, 1048-1057 (2001)
3. Wagner, K., Follette, K., Close, L. M., et al., Magellan Adaptive Optics Imaging of PDS 70: Measuring the Mass Accretion Rate of a Young Giant Planet within a Gapped Disk, *Astrophys. J. Lett.*, 863, L8 (2018)
4. Haffert, S., Bohn, A. J., de Boer, J., et al., Two Accreting Protoplanets Around the Young Star PDS 70, *Nat. Astron.*, 3, 749 (2019)
5. Van Holstein, R. G., Bos, S., Ruigrok, J., Calibration of the instrumental polarization effects of SCEXAO-CHARIS' spectropolarimetric mode, *Proc. SPIE*, 11447, 114475B (2020)
6. Currie, T. Brandt, T., Uyama, T., SCEXAO/CHARIS Near-infrared Direct Imaging, Spectroscopy, and Forward-Modeling of κ And b: A Likely Young, Low-gravity Superjovian Companion, *Astron. J.*, 156, 291 (2018)
7. Milli, J., Mouillet, D., Lagrange, A.-M., et al., Impact of angular differential imaging on circumstellar disk images, *Astron. Astrophys.*, 545, 111 (2012)
8. Cox, C., Ritchie, E., Bergeron, J. M., Noll, K., NICMOS Distortion Correction, *Instrument Science Report*, OSG-CAL-97-07 (1997)
9. Service, M., Lu, J. R., Campbell, R., et al., A New Distortion Solution for NIRC2 on the Keck II Telescope, *Publ. Astron. Soc. Pac.*, 128, 5004 (2016)
10. Grady, C., Woodgate, B., Bruhweiler, F. et al., Hubble Space Telescope Space Telescope Imaging Spectrograph Coronagraphic Imaging of the Herbig AE Star AB Aurigae, *Astrophys. J. Lett.*, 523, L151 (1999)
11. Brandenburg, A., Dobler, W., Hydromagnetic turbulence in Computer Simulations, *Computer Physics Communications*, 147, 471-475 (2002)
12. Haugen, N., Brandenburg, A., Dobler, W., Simulations of nonhelical hydromagnetic turbulence, *Phys. Rev. E.*, 70, 016308 (2004)
13. Lyra, W., Johansen, A., Klahr, H., Global magnetohydrodynamical models of turbulence in protoplanetary disks. I. A cylindrical potential on a Cartesian grid and transport of solids, *Astron. Astrophys.*, 479, 883-901 (2008)
14. McNally, C. P., Lyra, W., Passy, J.-C., A Well-posed Kelvin-Helmholtz Instability Test and Comparison, *Astrophys. J. Suppl. Ser.*, 201, 18 (2012)
15. Baruteau, C., Masset, F., Type I Planetary Migration in a Self-Gravitating Disk, *Astrophys. J.*, 678, 483-497 (2008)
16. Lodato, G., Classic disc physics, *New Astronomy Reviews*, 52, 21-41 (2008)
17. Dullemond, C., Juhasz, A., Pohl, A., RADMC-3D: A multi-purpose radiative transfer tool, *Astrophysics Source Code Library*, record ascl:1202.015 (2012)
18. Hord, B., Lyra, W., Flock, M., On Shocks Driven by High-mass Planets in Radiatively Inefficient Disks. III. Observational Signatures in Thermal Emission and Scattered Light, *Astrophys. J.*, 849, 164 (2017)
19. Preibisch, T., Ossenkopf, V., Yorke, H., The influence of ice-coated grains on protostellar spectra, *Astron. Astrophys.*, 279, 577 (1993)

20. Boss, A., Evolution of the Solar Nebula. IV. Giant Gaseous Protoplanet Formation, *Astrophys. J.*, 503, 923-937 (1998)
- 21.. Szulagyi, J., Mayer, L., Quinn, T., Circumplanetary discs around young giant planets: a comparison between core-accretion and disc instability, *Mon. Not. R. Astron. Soc.*, 464, 3158 (2017)
22. Zhu, Z., Hartmann, L., Nelson, R. P., Challenges in Forming Planets by Gravitational Instability: Disk Irradiation and Clump Migration, Accretion, and Tidal Destruction, *Astrophys. J.*, 746, 110 (2012)
23. Vorobyov, E., Elbakyan, V., Gravitational fragmentation and formation of giant protoplanets on orbits of tens of au, *Astron. Astrophys.*, 618, 7 (2018)
24. Vorobyov, E., Elbakyan, V., Gravitoviscous protoplanetary disks with a dust component. II. Spatial distribution and growth of dust in a clumpy disk, *Astron. Astrophys.*, 631, 1 (2019)
25. Cadman, J., Rice, K., Hall, C., AB Aurigae: possible evidence of planet formation through the gravitational instability, *Mon. Not. R. Astron. Soc.*, 504, 2877 (2021)
26. Szulagyi, J., Masset, F., Lega, E., et al., Circumplanetary disc or circumplanetary envelope?, *Mon. Not. R. Astron. Soc.*, 460, 2853 (2016)
27. Currie, T., Burrows, A., Madhusudhan, N., et al., A Combined Very Large Telescope and Gemini Study of the Atmosphere of the Directly Imaged Planet, β Pictoris b, *Astrophys. J.*, 776, 15 (2013)
28. Boccaletti, A., Di Folco, E., Pantin, E., et al., Possible evidence of ongoing planet formation in AB Aurigae. A showcase of the SPHERE/ALMA synergy, *Astron. Astrophys.*, 637, L5 (2020)
29. Betti, S. K., Follette, K., Jorquera, S., et al., Detection of Near-Infrared Water Ice at the Surface of the (pre)Transitional Disk of AB Aur: Informing Icy Grain Abundance, Composition, and Size, arxiv:2201.08868 (2022)
30. Jorquera, S., Bonnefoy, M., Betti, S. K., et al., LBT search for companions and sub-structures in the (pre)transitional disk of AB Aurigae, arxiv:2201.08867 (2022)
31. Keppler, M., Benisty, M., Mueller, A., et al., Discovery of a planetary-mass companion within the gap of the transition disk around PDS 70, *Astron. Astrophys.*, 617, A44 (2018)
32. Sallum, S., Follette, K., Eisner, J. A., Accreting protoplanets in the LkCa 15 transition disk, *Nature*, 527, 342 (2015)
33. Kraus, A., Ireland, M., LkCa 15: A Young Exoplanet Caught at Formation?, *Astrophys. J.*, 745, 5 (2012)
34. Currie, T., Marois, C., Cieza, L., et al., No Clear, Direct Evidence for Multiple Protoplanets Orbiting LkCa 15: LkCa 15 bcd are Likely Inner Disk Signals, *Astrophys. J. Lett.*, 877, L3 (2019)
35. Mendigutia, I., Oudmaijer, R. D., Schneider, P. C., Spectro-astrometry of the pre-transitional star LkCa 15 does not reveal an accreting planet but extended H α emission, *Astron. Astrophys.*, 618, L9 (2018)
36. Quanz, S. P., Amara, A., Meyer, M. R., et al., A Young Protoplanet Candidate Embedded in the Circumstellar Disk of HD 100546, *Astrophys. J. Lett.*, 766, L1 (2013)
37. Quanz, S. P., Amara, A., Meyer, M. R., et al., Confirmation and Characterization of the Protoplanet HD 100546 b – Direct Evidence of Gas Giant Planet Formation at 50 au, *Astrophys. J.*, 807, 64 (2015)

38. Currie, T., Cloutier, R., Brittain, S., et al., Resolving the HD 100546 Protoplanetary System with the Gemini Planet Imager: Evidence for Multiple Forming, Accreting Planets, *Astrophys. J. Lett.*, 814, L27 (2015)
39. Rameau, J., Follette, K. B., Pueyo, L., et al., An Optical/Near-infrared Investigatino of HD 100546 b with the Gemini Planet Imager and MagAO, *Astron. J.*, 153, 244 (2017)
40. Brittain, S. D., Najita, J.R., Carr, J.S., High-resolution Near-infrared Spectroscopy of HD 100546. IV. Orbiting Companion Disappears on Schedule, *Astrophys. J.*, 833, 37 (2019)
41. Reggiani, M., Christiaens, V., Absil, O., et al., Discovery of a point-like source and a third spiral arm in the transition disk around the Herbig Ae star MWC 758, *Astron. Astrophys.*, 611, A74 (2018)
42. Wagner, K., Stone, J. M., Spalding, E., et al., Thermal Infrared Imaging of MWC 758 with the Large Binocular Telescope: Planetary-driven Spiral Arms?, *Astrophys. J.*, 882, 20 (2019)
43. Boccaletti, A., Pantin, E., Menard, F., et al., Investigating point sources in MWC 758 with SPHERE, *Astron. Astrophys.*, 652, L8 (2021)